Searching for primordial black holes with the Einstein Telescope: Impact of design and systematics

Gabriele Franciolini[1,2] Francesco Iacovelli[3,4] Michele Mancarella[5,6] Michele Maggiore[3,4]
Paolo Pani[1,2] and Antonio Riotto[3,4]

[1]*Dipartimento di Fisica, Sapienza Università di Roma, Piazzale Aldo Moro 5, 00185, Roma, Italy*
[2]*INFN, Sezione di Roma, Piazzale Aldo Moro 2, 00185, Roma, Italy*
[3]*Département de Physique Théorique, Université de Genève, 24 quai Ansermet,
CH-1211 Genève 4, Switzerland*
[4]*Gravitational Wave Science Center (GWSC), Université de Genève, CH-1211 Geneva, Switzerland*
[5]*Dipartimento di Fisica "G. Occhialini," Universitá degli Studi di Milano-Bicocca,
Piazza della Scienza 3, 20126 Milano, Italy*
[6]*INFN, Sezione di Milano-Bicocca, Piazza della Scienza 3, 20126 Milano, Italy*

Primordial black holes (PBHs) have recently attracted much attention, as they may explain some of the LIGO/Virgo/KAGRA observations and significantly contribute to the dark matter in our Universe. The next generation of gravitational wave detectors will have the unique opportunity to set stringent bounds on this putative population of objects. Focusing on the Einstein Telescope (ET), in this paper we analyze in detail the impact of systematics and different detector designs on our future capability of observing key quantities that would allow us to discover and/or constrain a population of PBH mergers. We also perform a population analysis, with a mass and redshift distribution compatible with the current observational bounds. Our results indicate that ET alone can reach an exquisite level of accuracy on the key observables considered as well as detect up to tens of thousands of PBH binaries per year (*for an optimistic PBH population that saturates current upper bounds on the abundance*), but for some key signatures—in particular, high-redshift sources—the cryogenic instrument optimized for low frequencies turns out to be crucial, for both the number of observations and the error on the parameter reconstruction. As far as the detector geometry is concerned, we find that a network consisting of two separated L-shaped interferometers of 15 (20) km arm length, oriented at 45° with respect to each other, performs better than a single triangular-shaped instrument of 10 (15) km arm length, for all the metrics considered.

I. INTRODUCTION

The detection of gravitational waves (GWs) [1] performed by the LIGO/Virgo/KAGRA (LVK) Collaboration opened up a new way for us to observe nature [2–5]. Such discovery brings us information on the compact objects populating our Universe and will allow us to learn how they formed (see, e.g., Refs. [6,7] for recent reviews).

A particularly interesting population of objects is represented by primordial black holes (PBHs). PBHs can form out of the collapse of extreme inhomogeneities existing during the radiation-dominated era [8–11] and can possess a wide range of masses [12–15]. While several constraints were set on their abundance, they are still allowed to explain the entirety of the dark matter in our Universe in certain mass ranges (see [16] for a review). Besides the connection to the dark matter problem, PBHs could be the seed of supermassive black holes at high redshift [17–19] and contribute to a fraction of the BH merger events already discovered by LIGO, Virgo, and KAGRA detectors

[20–51] (see Refs. [52–54] for reviews on PBH mergers as GW sources).

It is exciting that future GW detectors, such as the third-generation (3G) ground-based interferometers, Einstein Telescope (ET) [55–57] and Cosmic Explorer (CE) [58,59], and the future space mission Laser Interferometer Space Antenna [60], could enhance our capabilities to search for GW signatures of PBHs. ET and CE are expected to reach much higher sensitivities than current detectors and have a rich science case [61,62]. In particular, for compact binary coalescences, they will allow for detection rates larger by orders of magnitude compared to current detectors, with $\mathcal{O}(10^4-10^5)$ binary black holes (BBHs) and binary neutron stars detected per year, and more accurate measurements for "golden" events with a high signal-to-noise ratio (SNR) [63,64]. Furthermore, 3G detectors will allow for entirely new tests on the existence of a population of PBHs [42,65–70].

We are currently experiencing a crucial stage of the development of 3G detector projects, in which the

community is consolidating the science case,[1] and PBHs may play an important role in such an endeavor. Following the recent evolution of our understanding of the physics of PBH mergers (see Ref. [69] and references therein), the main goal of this paper is to provide a systematic analysis of the performance, with respect to PBH searches, of different detector designs under consideration within the ET Collaboration. In particular, we will highlight which features of the proposed future detector are essential in order to fully exploit its capability of searching for PBHs. The main results of this analysis were included in the official document of the ET Collaboration presenting the full study of how the science case of ET depends on different options for the detector design [72].

In Sec. II, we briefly summarize the discriminators which can be used to determine the origin of a merger, based on the observed redshift, masses, spins, eccentricity, and tidal deformability [69]. In Sec. III, we describe the ET designs we considered, following Ref. [72], while in Sec. IV we introduce our methodology. Our results focusing on some specific PBH signatures are summarized in Sec. V, where we present a detailed comparison between the different designs when key observables are considered. In Sec. VI, we shift our focus on a comparison of performance adopting population analysis, considering as a benchmark the recent upper bound on the PBH population based on gravitational wave transient catalog (GWTC-3) data, derived in Ref. [50]. Finally, we conclude in Sec. VII with a summary of our findings and a discussion of future research directions.

We will consider binaries with individual component masses in the range between $\mathcal{O}(10^{-2})M_\odot$ and $\mathcal{O}(10^3)M_\odot$, which are among the main targets for ET, greatly extending the reach of current LVK searches. Throughout this paper, we adopt geometrical units ($G = c = 1$). We denote binary components with masses m_1 and m_2, mass ratio $q = m_2/m_1 \leq 1$, total mass $M = m_1 + m_2$, dimensionless spins χ_i (with $0 \leq \chi_i \leq 1$), and at redshift z.

II. KEY PREDICTIONS FOR PBH MERGERS

In this section, we give a summary of the main predictions of PBH models, focusing on mergers in the stellar mass range, which are the prime target of ET searches. We refer the reader to Ref. [69] and references therein for more details.

Throughout this work, we consider the standard PBH formation mechanism and assume that PBHs are generated from the collapse of sizable cosmological perturbations in the radiation-dominated epoch of the early Universe [12–15]. In this scenario, PBHs are predicted to be characterized by small natal spins [73,74] and are not

clustered at high redshift [75–80]. Alternative scenarios, such as the formation from the collapse of particles, Q-balls, oscillons, domain walls, and heavy quarks of a confining gauge theory, may lead to different predictions for the PBH spin at formation [81–85]. We remark that the impact of accretion (when relevant) onto the mass-spin correlation and the properties of other observables (i.e., redshift distribution, eccentricity, and masses) remain the same as for the standard scenario (see Ref. [69] for more details).

A. Redshift

It can be shown that the merger rate of PBHs is dominated by binaries formed in the early Universe via gravitational decoupling from the Hubble flow well before the matter-radiation equality [86,87]. Other dynamical formation channels are possible, i.e., the formation of binaries taking place in present-day halos through gravitational capture or three-body interactions [88], but those are subdominant contributions in the parameter space we consider in this work [25,31,80,89]. In contrast to the astrophysical channels, the merger rate density of such a population of primordial BBHs monotonically increases with redshift as [25,27,34]

$$\mathcal{R}_{\text{PBH}}(z) \propto \left[\frac{t(z)}{t(z=0)}\right]^{-34/37}, \qquad (1)$$

extending up to redshifts $z \gtrsim \mathcal{O}(10^3)$. We stress that the evolution of the merger rate shown in Eq. (1) is dictated by how pairs of PBHs decouple from the Hubble flow before the matter-radiation equality era. Therefore, Eq. (1) is a robust feature of the PBH channel.

High-redshift mergers are difficult to produce within the context of astrophysical channels. In particular, a conservative threshold above which no astrophysical mergers can exist can be set at $z \gtrsim 30$ within standard cosmologies [90]. It should be stressed that, even though the epoch of first star formation is poorly known, theoretical calculations and cosmological simulations suggest this should fall below $z \sim 40$ [90–97] (see also Refs. [98,99], where pop III star formation was suggested to start at different epochs). In addition, a crude estimate for the time delay between pop III star formation and the subsequent BBH mergers can be derived from the result of population synthesis models and gives roughly $\mathcal{O}(10\,\text{Myr})$ [97,100–108]. Therefore, we consider merger redshifts $z \gtrsim 30$ to be smoking guns for primordial binaries [42,70,90,109–111].

B. Masses and spins

The distribution of PBH masses m_{PBH} is determined by both the characteristic size and statistical properties of the density perturbations, which are directly inherited from the spectrum of curvature perturbations generated during the inflationary epoch, and the PBH threshold for collapse,

---

[1]For a repository of papers relevant for ET, produced in the context of the activities of the ET Observational Science Board, see Ref. [71].

which retains a dependence on the thermal history [50,51,112–115].

One of the most important properties of PBHs is that they could populate the subsolar-mass range and the supposed astrophysical mass gaps [37,50,116]. Depending on the PBH mass one considers, different strategies could be adopted to distinguish PBHs from other astrophysical contaminants. In the following, we discuss the most informative as a function of the mass range.

In the subsolar range, only the primordial scenario or beyond standard model physics (e.g., dark sector interactions [117]) can produce binary BHs. However, other exotic compact objects [118] (e.g., boson stars [119]) may also contaminate the signals. These classes of objects could be distinguished by focusing on the tidal disruption and tidal deformability measurements, which are absent for BBHs (see Sec. II D below).

Just above the solar mass, PBHs can be confused with neutron stars (NSs). Once again, tidal deformability measurement should be used to break the degeneracy between these two classes of objects. Additionally, solar-mass BHs can form out of NS transmutation in certain particle–dark-matter scenarios [120–127] or asteroid-mass PBH dark matter [128]. Also, some component BHs in binaries may form out of previous NS-NS mergers and then pair again to produce a light binary [129]. In such a case, the second-generation BH formed is expected to be spinning [130], in contrast with the prediction for the PBH scenario in this mass range, as we shall see.

When focusing on even larger masses ($\gtrsim 3 M_\odot$), individual PBH mergers can be distinguished from stellar-origin BHs only by using the information on mass-spin correlations. At high redshift, PBHs are expected to be produced with negligible spin. This is due to a combination of factors. Extreme Gaussian perturbations tend to have nearly spherical shape [131] and the collapse takes place in a radiation-dominated universe, which means that over-densities that collapse to form PBHs evolve fast enough that torques are not able to spin up the collapsing over-density. As a consequence, the initial dimensionless Kerr parameter $\chi \equiv J/M^2$ (where J and M are the angular momentum and mass of the BH, respectively) is expected to be below the percent level [73,74]. However, a non-vanishing spin can be acquired by PBHs forming binaries through an efficient phase of accretion [132] prior to the reionization epoch.

Accretion was shown to be efficient only for PBHs with masses above $m_{PBH} \gtrsim \mathcal{O}(10 M_\odot)$ [132]. Therefore, the PBH model is characterized by binary components with negligible spins in the "light" portion of the observable mass range of current ground-based detectors. At larger masses, the PBH model predicts a characteristic correlation between large binary total masses and large values of the spins of their PBH constituents. This correlation is induced by accretion effects and is subject to the uncertainties of the

accretion models (see a detailed discussion on this in Ref. [34]). In addition, the spin directions of PBHs in binaries are assumed to be independent and randomly distributed on the sphere in Ref. [34]. We will consider this scenario in the rest of the paper, but we warn the reader that details of the accretion dynamics remain uncertain. We refer to Ref. [69] for an analytic fit of the relation between the PBH masses and spins as a function of parametrized uncertainties of the accretion efficiency.

C. Eccentricity

Another key prediction of the primordial BH model involves the eccentricity e of PBH binaries. While formed with large eccentricity at high redshift, PBH binaries then have enough time to circularize before the GW signal can enter the observation band of current and future detectors.[2] Let us clarify this statement.

One can show that the differential probability distribution of the rescaled angular momentum $j \equiv \sqrt{1-e^2}$ parametrically behaves as [25,141,142]

$$P(j) = 4j\left(\frac{x}{\bar{x}}\right)^3 \left[\frac{[1+(\sigma_M^2/f_{PBH}^2)]^{1/3}}{4j^2 + [1+(\sigma_M^2/f_{PBH}^2)](\frac{x}{\bar{x}})^6}\right]^{3/2}, \quad (2)$$

where $\sigma_M \simeq 0.004$ indicates the variance of the Gaussian large-scale density perturbations at matter-radiation equality, x stands for the comoving distance between the two PBH forming the binary, while $\bar{x}$ is its average distance in the early Universe. This distribution results from the effect of both surrounding PBHs and matter perturbations acting with a torque on the PBH binary during its formation. Slight refinements to this high-redshift distribution were derived in Ref. [27], but this does not affect our main argument here.

The crucial point is the following. Even though the high-redshift distribution of j peaks at small values (i.e., high eccentricities), PBH binaries spend a large portion of the age of the Universe inspiraling. Such a phase drives the eccentricity toward much smaller values. We can rearrange the equations that describe the orbital evolution under the effect of GW emission and define the pericenter distance $r_p \equiv a(1-e)$, with a denoting the semimajor axis, to find [143]

---

[2]Notice that Refs. [133,134] considered PBH binaries from dynamical assembly in the late-time Universe that retain large eccentricities, comparable to expectations from the astrophysical dynamical formation scenarios. This mechanism, however, provides a subdominant contribution to the overall merger rate in the standard scenario [25,88]. This situation may be realized with strong PBH clustering suppressing the early-Universe binary merger rate while enhancing the late-time Universe contribution [31,80,135,136]. However, we stress that this scenario would require a large value of the PBH abundance ($f_{PBH} \simeq 1$), which is in contrast with current PBH constraints in the LIGO-Virgo-KAGRA detector mass range [16] (see also the recent results of Refs. [50,137–140]).

$$\frac{d \ln e}{d \ln r_p} = \frac{(1+e)(304+121e^2)}{192-112e+168e^2+47e^3} \approx 1.6 + \mathcal{O}(e). \quad (3)$$

Let us make a concrete example to gain intuition. For a characteristic PBH binary formed by a narrow PBH population with $f_{PBH} = 10^{-3}$ and $m_{PBH} = 30M_\odot$ and expected to merge within a Hubble time at $z \simeq 0$, one obtains a characteristic initial binary pericenter distance to be $r_p \approx 4 \times 10^6$ km. We recall that the binary would enter the ET and *second-generation observable band* when its frequency becomes of the order of a few hertz and 10 Hz, respectively. These frequencies correspond roughly to

$$\text{LVK: } r_p \simeq 22R_{Sch} \simeq 2 \times 10^3 \text{ km,}$$

$$\text{ET: } r_p \simeq 102R_{Sch} \simeq 9 \times 10^3 \text{ km,}$$

for $m_{PBH} = 30M_\odot$. Then, using Eq. (3), one finds that the observable eccentricity of the orbit is reduced below $e \approx 10^{-5}$.

In other words, when the binary enters the detectable frequency band of GW experiments, it is expected to have circularized its orbit to such an extent that the remaining eccentricity is not detectable. This property can be exploited to distinguish primordial binaries from those produced by astrophysical scenarios. While isolated formation channels predict small values of e in the observable range of frequencies of 3G detectors, dynamical channels predict a fraction $\mathcal{O}(10\%)$ with $e > 0.1$ [88,144–149]. This can be used to distinguish the origin of the latter class of compact objects (see, e.g., [150–155]). Therefore, reaching a sensitivity to e below around 10^{-1} indicates the possibility of performing tests on the formation pathway of a binary.

D. Tidal deformability

PBHs lighter than a few solar masses are easily distinguished from (heavier) stellar-origin BHs. However, other compact objects might contaminate the solar- and subsolar-mass range. For example, in standard astrophysical scenarios, white dwarfs and NSs are formed with masses above $\approx 0.2M_\odot$ [156] and $\approx 1M_\odot$ [157–160], respectively.

One simple discriminator between PBHs and other compact objects is provided by the Roche radius r_{Roche}, defined as the minimum orbital distance below which the secondary object gets tidally disrupted, if it is not a BH. The Roche radius is approximately defined as $r_{Roche} \sim 1.26r_2q^{-1/3}$, in terms of the radius of the secondary object r_2 and the mass ratio $q = m_2/m_1$. When r_{Roche} is greater than the radius of the innermost stable circular orbit (ISCO), $r_{Roche} > r_{ISCO} \sim \mathcal{O}(M)$, the binary gets tidally disrupted before the merger. The GW signature of such an event would be characterized by an effective cutoff of the GW signal at the frequency corresponding to r_{Roche}.

Based on these estimates, one can expect less compact objects, like brown and white dwarfs, to be tidally disrupted well before the contact frequency.

Other (exotic) compact objects [118] (e.g., boson stars [161]) would provide another possible explanation for a (sub)solar compact object. However, whether or not they get disrupted before the ISCO frequency depends on their compactness. For example, the vanilla "mini" boson star model without self-interactions [162] with masses around the solar-mass range would be tidally disrupted before the ISCO (see also Ref. [69]). On the other hand, in the presence of strong scalar self-interactions, boson stars can be as compact as a NS [163,164], and the tidal disruption is not a clear-cut discriminator.

In this paper, to compare the performance of different detector configurations, we will focus on another key discriminator between PBHs and (sub)solar horizonless objects, that is, the absence, in the former case, of tidal deformability contributions to the gravitational waveform. The tidal Love numbers are predicted to be vanishing for a BH [165–178], whereas they are generically nonzero and model dependent for any other compact object [164]. The tidal Love numbers enter the GW phase starting at 5 post-Newtonian (PN) order, with the 5PN and 6PN contributions being linearly related to the dominant quadrupolar tidal Love number $\lambda_2^{(i)} = 2m_i^5 k_2^{(i)}/3$ of the ith body [179,180]. In the Newtonian approximation, the tidal Love number of an object is (see, e.g., [181])

$$k_2^{(i)} \sim \mathcal{O}(0.01\text{–}0.1)\left(\frac{r_i}{m_i}\right)^5, \quad (4)$$

where the precise value of the dimensionless prefactor depends on the nature of the object (i.e., in the case of a NS, on the equation of state). Therefore, less compact objects are characterized by a larger tidal deformability and would be more easily distinguished from a (P)BH.[3]

III. ET DETECTOR DESIGNS AND NETWORKS

In this section, we provide a short summary of the different designs and detector networks considered in this study. For more details, we direct the reader to the official ET document presenting the full scientific part of the study of how the science output changes with the detector design, performed in Ref. [72].

We will consider three main geometries for ET: the triangular geometry (Δ), consisting of three nested detectors with 60° arm aperture, a network of two L-shaped

---

[3]A further discriminator could be tidal heating corrections to the waveform in the case of BHs, which is due to dissipation at the event horizon [182] while remaining negligible for other compact objects [118,183]. However, tidal heating is generically subdominant with respect to the tidal deformability correction presented above. Therefore, we do not include it in our analysis.

detectors (i.e., with 90° arm aperture) with parallel arms (2L-0°) and a network of two L-shaped detectors with misaligned arms (2L-45°).[4] Among the configurations consisting of two well-separated L-shaped detectors, the parallel one has the advantage of maximizing the sensitivity to stochastic backgrounds and can result in a higher SNR for some of the observed sources, while the misaligned one has no blind spots and is optimal in terms of accuracy on the reconstruction of the sky position and distance of the detected events. Regarding the sites of the detectors, there are two main candidates by the time of writing: the Sos Enattos site in Sardinia, Italy, and the Meuse-Rhine Euroregion across Belgium, Germany, and the Netherlands.[5] When considering a single triangular instrument, we choose for definiteness the Sardinia site (no major difference is expected if choosing the Meuse-Rhine site), while for the 2L configurations, we place one of the detectors in Sardinia and one in Meuse-Rhine.

On top of studying different geometries, as done in Ref. [72] we will consider different arm lengths for the detectors—namely, 10 and 15 km for the triangular geometry and 15 and 20 km for the 2L geometries—and two different scenarios: one in which the so-called "xylophone" design is employed, with each detector actually consisting of two interferometers—one optimized for low-frequency (LF) sensitivity (operating at cryogenic temperature) and the other for high-frequency (HF) sensitivity (we will refer to this configuration as HFLF-Cryo)—and a pessimistic scenario in which only the high-frequency optimized instrument will be operating (we will refer to this configuration as HF). Considering a sort of "intermediate" scenario, in which the detectors exploit the xylophone design with the LF instrument operating at room temperature, the results would be intermediate among the ones we will show for the HFLF-Cryo and HF scenarios.

The different amplitude spectral densities (ASDs) employed in the various cases are reported in Fig. 1, where we further show the ET-D sensitivity curve for comparison.[6] These curves have been provided by the ET Instrument Science Board and are an update of the ET-D curve, reflecting more detailed data on the technology used in the ET-D design.[7] It should be stressed that in this phase of the ET development the sensitivity curves are still in evolution and will continue to evolve, so these ASDs must be taken as
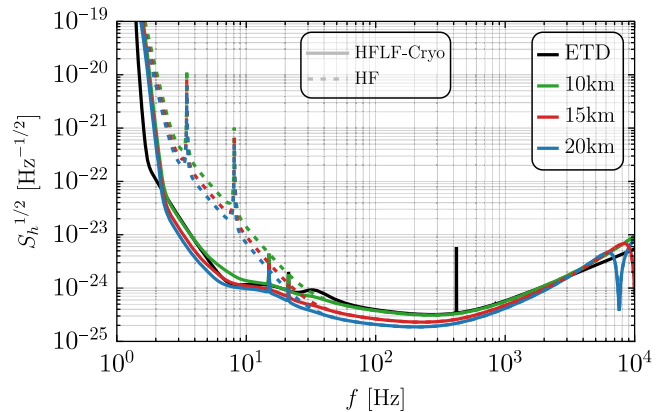

FIG. 1. Amplitude spectral densities for the various configurations considered in this work. Solid and dashed lines correspond to cryogenic low-frequency and high-frequency-only designs, respectively. We also show the ET-D design in black for comparison.

examples, within a range of other possibilities currently under study.

In Sec. VI, we will further compare with the results that can be obtained using a single L-shaped instrument of 20 km (placed for definiteness in the Meuse-Rhine site) as well as for ET (in its different geometries) as part of a 3G network, both with a single CE detector with 40 km arms and two CE instruments with 40 and 20 km arms, which is the preferred CE design at the moment [59,187].[8] We will also consider the current network of second-generation (2G) detectors, namely, the two LIGO detectors, Virgo and KAGRA, also including LIGO India (LVKI network) with ASDs representative of the best forecasted sensitivity for the upcoming fifth observing run (O5) [190].[9]

IV. SIGNAL-TO-NOISE RATIO AND FISHER MATRIX: NOTATION AND SETUP

Our analysis will focus on two complementary aspects of GW detections, which are our capability of detecting a particular source and the precision one can achieve at determining the source parameters. As we shall see, both aspects are crucial to chart future capabilities to search for the elusive population of PBHs. We will set ourselves in a simplified setting. In order to determine the detectability of a source, we will set a threshold for detection on the SNR. Regarding the measurability of source properties, the Fisher information matrix (FIM) is often used to assess the parameter estimation capabilities of GW detectors

---

[4]Notice that the notion of parallel and misaligned has to be intended with respect to the local East rather than with reference to the great circle connecting the detectors. See Sec. II and Appendix A in Ref. [72] for further discussion regarding this choice.

[5]For the Sardinia site, the chosen example coordinates are [lat = 40°31′0″, long = 9°25′0″], while for the Meuse-Rhine site [lat = 50°43′23″, long = 5°55′14″].

[6]The ET-D sensitivity curve is available [184].

[7]The curves are available [185] and are obtained using the PyGWINC package [186].

[8]For the CE detectors, we choose the same coordinates reported in Table III in Ref. [188] for the U.S. sites, locating the 40 km instrument in Idaho [lat = 43°49′36″, long = −112°49′30″] and the 20 km instrument in New Mexico [lat = 33°9′36″, long = −106°28′49″]. The latest CE sensitivity curves are available [189].

[9]The ASD files are available [191].

(see, for example, Refs. [164,192–197], as well as Refs. [198,199] for discussions of the limitations of this approach). While realistic performance may deviate from what is estimated on the basis of SNR and FIM, we expect such metrics to provide a consistent framework to compare various detector designs, following the aim of this project. Here, in order to compute the expected SNR and the FIM, we adopt the publicly available code GWFAST developed by some of the authors [64,200].[10,11]

The output $s(t)$ of a general GW interferometer can be written as the sum of the GW signal $h(t, \vec{\theta})$ and the detector noise $n(t)$, assumed to be Gaussian and stationary with zero mean. The posterior distribution for the hyperparameters θ can be approximated by

$$p(\theta|s) \propto \pi(\theta) \exp\left\{-\frac{1}{2}(h(\theta) - s|h(\theta) - s)\right\}, \quad (5)$$

in terms of the prior distribution $\pi(\theta)$. Here, we have introduced the inner product

$$(g|h) = 4\mathrm{Re} \int_{f_{\min}}^{f_{\max}} \frac{\tilde{g}^*(f)\tilde{h}(f)}{S_n(f)} \mathrm{d}f. \quad (6)$$

In Eq. (6), the tilde denotes a temporal Fourier transform and $S_n(f)$ is the detector noise power spectral density, while $f_{\min}$ and $f_{\max}$ are the detector minimum and maximum frequency of integration, respectively. One can, therefore, define the SNR as

$$\mathrm{SNR} \equiv \sqrt{(h|h)}. \quad (7)$$

In the limit of large SNR, one can perform a Taylor expansion of Eq. (5) and get

$$p(\theta|s) \propto \pi(\theta) \exp\left\{-\frac{1}{2}\Gamma_{ab}\Delta\theta^a\Delta\theta^b\right\}, \quad (8)$$

where $\Delta\theta = \theta_{\mathrm{p}} - \theta$ and we neglected noise-dependent factors restricting to the statistical uncertainty. In this setup, θ_{p} represents the posterior mean values, that also coincides with the true binary parameter $\theta_p = \theta_{\mathrm{true}}$. Also, we have introduced the Fisher matrix

$$\Gamma_{ab} \equiv \left(\frac{\partial h}{\partial \theta^a}\Big| \frac{\partial h}{\partial \theta^b}\right)_{\theta=\theta_{\mathrm{p}}}. \quad (9)$$

The errors on the hyperparameters (that represent a measure of the width of the posterior distribution) are, therefore,

given by $\sigma_a = \sqrt{\Sigma^{aa}}$, where $\Sigma^{ab} = (\Gamma^{-1})^{ab}$ is the covariance matrix.[12]

In the most general case, restricting to quasicircular orbits, the binary parameters are 15 for a BBH (see, e.g., [143]):

$$\theta_{\mathrm{BBH}} = \{\mathcal{M}_c, \eta, d_L, \theta, \phi, \iota, \psi, t_c, \Phi_c, \chi_{1,j}, \chi_{2,j}\}, \quad (10)$$

where $j = \{x, y, z\}$, extended to 18 in the case where one allows for tidal deformability of either components and orbital eccentricity:

$$\theta_\Lambda = \{\Lambda_1, \Lambda_2\}, \qquad \theta_e = \{e_0\}. \quad (11)$$

In particular, $\mathcal{M}_c$ denotes the detector-frame chirp mass, η the symmetric mass ratio, d_L the luminosity distance to the source, θ and ϕ the sky position coordinates, defined as $\theta = \pi/2 - \delta$ and $\phi = \alpha$ (with α and δ right ascension and declination, respectively), ι the inclination angle of the binary with respect to the line of sight, ψ the polarization angle, t_c the time of coalescence, Φ_c the phase at coalescence, $\chi_{i,j}$ the dimensionless spin of the object $i = \{1, 2\}$ along the axis $j = \{x, y, z\}$, and Λ_i the dimensionless tidal deformability of the object i, which is zero for a BH. A more convenient parametrization of tidal effects, which is the one we will use in the analysis, is given in terms of the quantities [206]

$$\tilde{\Lambda} = \frac{8}{13}[(1 + 7\eta - 31\eta^2)(\Lambda_1 + \Lambda_2)$$
$$+ \sqrt{1 - 4\eta}(1 + 9\eta - 11\eta^2)(\Lambda_1 - \Lambda_2)],$$
$$\delta\tilde{\Lambda} = \frac{1}{2}\left[\sqrt{1 - 4\eta}\left(1 - \frac{13272}{1319}\eta + \frac{8944}{1319}\eta^2\right)(\Lambda_1 + \Lambda_2)\right.$$
$$\left. + \left(1 - \frac{15910}{1319}\eta + \frac{32850}{1319}\eta^2 + \frac{3380}{1319}\eta^3\right)(\Lambda_1 - \Lambda_2)\right],$$
$$\quad (12)$$

which has the advantage that $\tilde{\Lambda}$ is the combination entering the waveform at 5PN and is, thus, better constrained than Λ_1 and Λ_2 separately, while $\delta\tilde{\Lambda}$ first enters at 6PN. Including also a small eccentricity in the orbit, there is one more parameter to consider, e_0, which denotes the eccentricity at a given reference frequency, which we fix at $f_{e_0} = 10$ Hz.

For the various analyses in Sec. V, we adopt different state-of-the-art waveform models. In Secs. V A and V B, we employ the inspiral-merger-ringdown (IMR) model

---

[10]The GWFAST code is available [201].

[11]Other parameter estimation codes, tuned toward 3G detectors, have been developed recently, in particular, GWBENCH [63,188], GWFISH [202], TiDoFM [203,204], and the code used in Ref. [205]. Results from these codes were cross-checked and are consistent with each other [64,72].

[12]For the results in Sec. V, we impose physical priors on the waveform parameters to overcome limitations in the Fisher matrix related to bad conditioning. In particular, we draw samples from the distribution in Eq. (8), use rejection sampling to enforce the prior, and compute the covariance of the remaining samples. The procedure is detailed in Appendix C in Ref. [64].
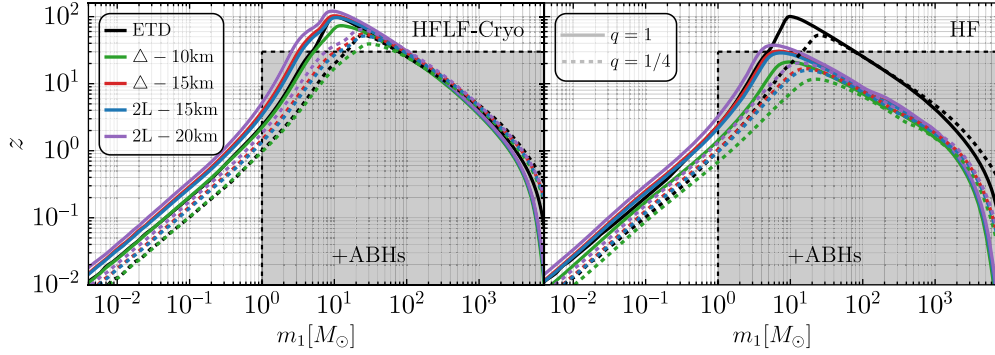
FIG. 2.   Horizon redshift z as a function of the primary mass for $q = 1$ (solid lines) and $q = 1/4$ (dashed lines). The left panel corresponds to the HFLF-Cryo configuration and the right panel to the HF configuration, while different colors indicate various geometries *of the network*. We also show the ET-D design for comparison, while the gray area delimits the subsolar $m_1 < M_\odot$ and $z > 30$ regions, which are PBH smoking-gun signatures. The binaries are assumed to be circular ($e_0 = 0$), and BH spins are assumed to be negligible ($\chi_1 = \chi_2 = 0$), as predicted by the PBH scenario. The shaded region marked "+ABH" denotes (approximately) the part of the mass-redshift plane to which astrophysical BBHs are confined. As a consequence of our choices ($\iota = 0°$ and optimal location), aligned and misaligned 2L configurations result in the same performance for this kind of estimation; we, thus, report only the 2L-45° case.

IMRPhenomHM, which includes the contribution of the higher-order harmonics $(l, m) = (2, 1), (3, 2), (3, 3), (4, 3)$, and $(4, 4)$ on top of the $(2, 2)$ quadrupole [207,208]; this neglects possible precession of sources, but it is justified in our case as high-redshift or light events are characterized by negligible spins in the PBH scenario.[13] In Sec. V C, we use the inspiral-only model TaylorF2 [209–211] with the extension to include a small orbital eccentricity presented in Ref. [212][14]; and in Sec. V D, we use in a broad mass range TaylorF2 with tidal terms at 5PN and 6PN [206] and spin-induced quadrupole moment [213] and the full inspiral-merger model IMRPhenomD_NRTidalv2 [214–216] in its tuning range. Finally, in Sec. V E and in the population analysis in Sec. VI, instead, we adopt the full IMR model IMRPhenomXPHM, which includes both the contribution of higher-order harmonics and precessing spins [217,218]. This choice is dictated again by the expectation of the PBH scenario, which does not predict tidal deformability effects nor sizable eccentricity for the detectable events.

V. RESULTS

In this section, we report our results, maintaining the structure described in Sec. II. We will also provide a summary of our results in the conclusions.

Throughout the work, we will report results for the various detector geometry and network with different colors while splitting the two configurations HFLF-Cryo and HF into left and right panels, respectively (see, e.g., Fig. 2). We also draw dense grid lines to guide the eye in the comparison of the various designs.

A. High-redshift measurements

High-redshift mergers are a prime target of 3G detector searches. In Fig. 2, we show the horizon redshift (defined as the maximum distance at which a source could be detected, assuming optimal alignment) in the whole spectrum of source-frame masses available to ET, i.e., $M \approx [10^{-2}, 10^4] M_\odot$. We assume equal-mass systems, negligible spins, and eccentricity, as expected for primordial BBHs, and set a threshold *network* SNR ≥ 8 for detection.

Two main trends limit the reach of ET. At small masses, GW amplitudes are reduced, and only sufficiently nearby sources can be loud enough to be detected. At higher masses, on the other side of the spectrum, a strong limitation comes from the intrinsically small frequencies spanned by the GW signal, which can exit the frequency spectrum to which ET is most sensitive. In particular, the detector frame ISCO frequency scales as

$$f_{\text{ISCO}}^{\text{det}} \approx 4.4 \text{ kHz} \left(\frac{M_\odot}{m_1^{\text{src}} + m_2^{\text{src}}} \right) \left(\frac{1}{1 + z} \right), \quad (13)$$

from which we clearly see that signals heavier than $M \gtrsim 10^2 M_\odot$ at redshift $z \gtrsim 10$ would end up at small, unreachable frequencies in the ET frame. This already indicates the importance of the LF implementation. To gain further intuition on the relevance of the LF instrument when searching high-redshift mergers, in Fig. 3 we compare

---

[13]Even though we are injecting spinless binaries in the section under consideration, adopting a waveform model which allows for only aligned spins reduces the number of parameters in the Fisher. We do not expect this to significantly impact our results, and it corresponds to parameter estimations that adopt physically motivated narrow spin priors.

[14]When using TaylorF2, we cut the inspiral phase at the ISCO frequency of a remnant Schwarzschild BH with mass $\approx M_{\text{tot}}$. Extending the Fisher analysis to higher frequencies would improve measurement errors but would also push the validity of the waveform model to its limit.
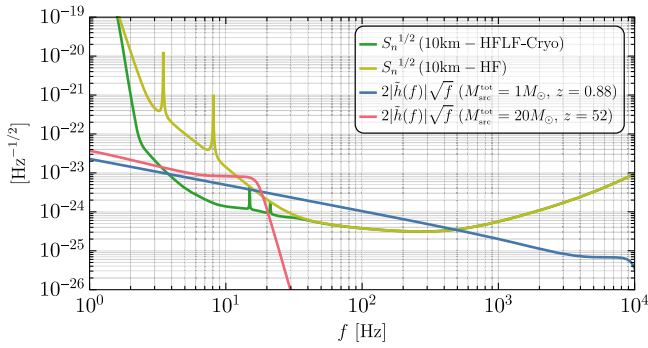
FIG. 3. Comparison between the amplitude of a PBH binary signal and the ET detector sensitivity curves shown in green (10 km-HFLF-Cryo) or yellow (10 km-HF). We consider a distant merger with source-frame mass $M_{src}^{tot} = 20 M_\odot$ at $z = 52$, reported in red. Also, we show in blue a subsolar merger with $M_{src}^{tot} = 1 M_\odot$ at $z = 0.88$. In both cases, we assume $q = 1$, optimal orientation of the binary, and the redshift is fixed in order to have SNR = 9 in the Δ-10 km-HFLF-Cryo configuration.

the signal amplitude for a merger with source-frame mass $M_{src}^{tot} = 20 M_\odot$ located close to the horizon (i.e., having SNR = 9 in the Δ-10 km-HFLF-Cryo configuration). Because of the large source redshift, the detector frame mass is redshifted by a large factor, and the majority of SNR can accumulate only in the LF portion of the sensitivity curve.

Looking at Fig. 2, we see that the reach of ET configurations can be only larger than $z \gtrsim 30$ (for a narrow window of masses $m_1 \approx [5, 10^2] M_\odot$ assuming $q \approx 1$) if the low-frequency instrument is implemented. In fact, the cryogenic implementation, with enhanced sensitivity at $f < 10$ Hz, provides the best design in terms of the number of distant detectable mergers.

The smoking-gun high-redshift signature can be employed (provided a sufficient precision is achieved when estimating the source redshift), when both individual event analyses are concerned [69,109,111], as well as population studies [70,110]. Based on a FIM metric, we compare the performance of different configurations in Fig. 4, which reports the maximum source redshift above which a relative precision on d_L better than 10% and 1% cannot be achieved for equal-mass nonspinning systems.[15]

As observed in terms of the horizon for detection, the relative error σ_{d_L}/d_L is strongly impacted by the performance of the detector configurations at low frequencies and follows the general trend observed in the behavior of the horizon; see Fig. 2. Longer detector arms lead to larger SNR and reduced uncertainties. At the same time, we observe comparable performance between the Δ-15 km and 2L-15 km, while 2L-20 km remains the best configuration we tested. Again, the absence of the low-frequency

---

[15]For a complementary visualization of the performance of different configurations, one may adopt the inference horizon introduced in Ref. [219].

instrument would lead to a drastic reduction in performance, which completely prevents the exploitation of the high-redshift signature to discover PBHs.

The same conclusion is supported by the population analysis presented in the following section (see, in particular, Table I).

B. Subsolar merger measurements

In this subsection, we focus on the second smoking-gun signature of PBHs, which is represented by the subsolar-mass window. ET will dramatically extend the reach of current technology when searching for mergers with at least one component below the Chandrasekhar limit [65,66].

In Fig. 2, we show the detection horizon also in the subsolar-mass range, i.e., the range of masses where only PBHs, white dwarfs, brown dwarfs, or exotic compact objects [118] can appear. For such masses, a large portion of the SNR is built up in the HF range of the sensitivity curve, so the horizons are only slightly dependent on the LF instrument. This is supported by Fig. 2, where, for subsolar masses, no significant difference in horizon redshift is observed between various configurations when removing the LF instrument. This can be understood by noticing that the GW signal of subsolar mergers can be observed only in its inspiral phase, which crosses the whole frequency range accessible to ET and the SNR is mainly dominated by the range of frequencies where the experiment is most sensitive, which remain fixed regardless of the presence of the LF instrument (see Fig. 1). This is also shown in Fig. 3, where we compare the signal amplitude for a subsolar merger with source-frame mass $M_{src}^{tot} = 1 M_\odot$ located close to the horizon (i.e., having SNR = 9 in the Δ-10 km-HFLF-Cryo configuration). One note of caution is in order here. While our considerations are based on SNR detection threshold, the actual matched-filtering search for GW signals is considerably more complex. In particular, in the case of light events, no merger signal is available and the SNR is accumulated throughout the inspiral, spanning over the sensitivity band. As such, our considerations here are based on a simplified metric, which anyway allows for a consistent comparison of designs.

In Fig. 5, we compare the performance of different ET configurations when measuring the source-frame mass and distance of subsolar PBH mergers. To perform a proper comparison between different designs, for each mass m_1, we assume a source located at the same distance, which is arbitrarily fixed in order to have SNR = 30 in the Δ-10 km HFLF-Cryo configuration. BHs spins are assumed to be negligible ($\chi_1 = \chi_2 = 0$), as predicted by the PBH scenario. We adopt the IMRPhenomHM waveform model and test both face-on ($\iota = 0$) and edge-on ($\iota = \pi/2$) binaries.

When measuring the primary mass, we observe a large precision improvement on σ_{m_1} going toward lighter masses. This is due to the larger number of cycles that the binary spends inspiraling within the observable band. In all the
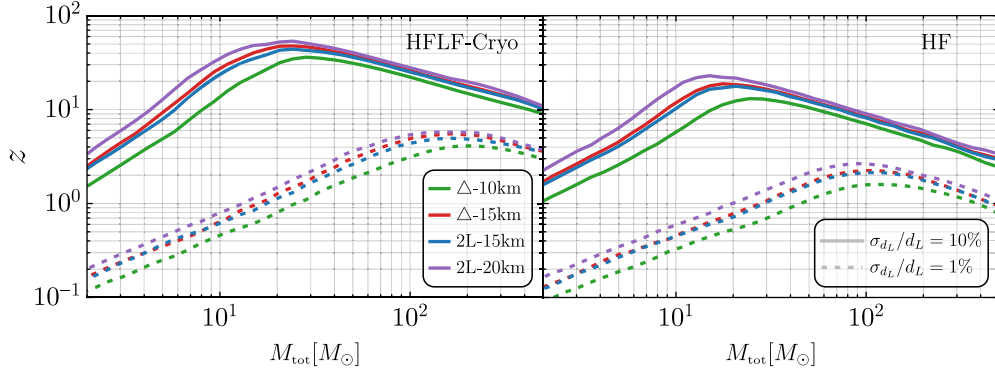
FIG. 4.   Contour lines of constant relative error as a function of source-frame total mass $M_{\rm tot}$ and source redshift z. Different colors indicate different configurations, while the left panel assumes HFLF-Cryo ASD and the right panel HF ASD. The solid (dashed) lines correspond to $\sigma_{d_L}/d_L = 10\%$ (1%). We assume equal masses $m_1 = m_2$, vanishing spins $\chi_1 = \chi_2 = 0$, and optimal orientation of the binary. We report only the 2L-45° case as in Fig. 2.

subsolar-mass range, a subpercent precision is achieved for sources with at least SNR $\gtrsim 30$, and the improvements in the LF sensitivity result in a minor gain of the precision on m_1 and z.

The conclusion is that, for subsolar-mass BHs, both the detection horizon and the accuracy on the source-frame mass and redshift reconstruction do not depend crucially on the LF sensitivity, and missing the LF instrument does not

TABLE I.   Top row: intrinsic number of PBH mergers per year predicted by the population we assume in this section. Bottom rows: number of detected events (SNR ≥ 12) per year for all the ET configurations considered in this work. In particular, in the second column we report the total number of detections, in the third the number of detections in the subsolar range (i.e., having at least the lightest object in the binary in the subsolar window $m_2 \leq 1M_\odot$), in the fourth and fifth the number of detections at high redshift, $z \geq 10$ and $z \geq 30$, respectively, in the sixth column the number of detected events having at least one of the masses in the so-called lower mass gap (i.e., $m_1 \in [2.5, 5]M_\odot$ and/or $m_2 \in [2.5, 5]M_\odot$), and in the last columns the number of observed events with at least one of the masses in the so-called upper mass gap (i.e., having at least the heavier object in the binary heavier than $m_1 \geq 50M_\odot$).

|	$N^{\rm tot}$	$N^{\rm SS}$	$N^{z>10}$	$N^{z>30}$	$N^{\rm LMG}$	$N^{\rm UMG}$
Intrinsic population	1 920 000	708 487	1 400 384	795 904	300 220	7774
Configuration	$N_{\rm det}^{\rm tot}$	$N_{\rm det}^{\rm SS}$	$N_{\rm det}^{z>10}$	$N_{\rm det}^{z>30}$	$N_{\rm det}^{\rm LMG}$	$N_{\rm det}^{\rm UMG}$
Δ-10 km-HFLF-Cryo	13 347	1650	336	17	2638	235
Δ-15 km-HFLF-Cryo	30 912	4281	1099	91	6443	376
2L-15 km-45°-HFLF-Cryo	24 900	3345	824	66	5132	332
2L-15 km-0°-HFLF-Cryo	26 585	3580	940	65	5517	356
2L-20 km-45°-HFLF-Cryo	35 524	5206	1434	140	7550	374
2L-20 km-0°-HFLF-Cryo	45 650	6745	1962	187	9809	465
1L-20 km-HFLF-Cryo	22 852	3019	698	37	4656	310
Δ-10 km-HF	4804	553	4	0	1023	74
Δ-15 km-HF	12 739	1660	106	0	2747	130
2L-15 km-45°-HF	10 714	1379	76	0	2239	113
2L-15 km-0°-HF	10 762	1374	79	0	2297	114
2L-20 km-45°-HF	20 704	2900	286	0	4574	175
2L-20 km-0°-HF	15 951	2211	210	0	3515	146
1L-20 km-HF	7610	987	51	0	1633	84
CE-40 km	41 650	6250	2050	142	8732	378
(CE-40 km)-(CE-20 km)	55 832	8702	2995	223	11 897	469
(CE-40 km)-(Δ-10 km-HFLF-Cryo)	56 964	8668	2876	226	12 108	510
(CE-40 km)-(2L-15 km-45°-HFLF-Cryo)	68 524	10 669	3604	331	14 713	590
(CE-40 km)-(2L-15 km-0°-HFLF-Cryo)	65 245	10 127	3366	294	13 990	563
(CE-40 km)-(CE-20 km)-(Δ-10 km-HFLF-Cryo)	71 414	11 300	3945	332	15 430	589
(CE-40 km)-(CE-20 km)-(2L-15 km-45°-HFLF-Cryo)	82 812	13 297	4757	443	17 975	663
(CE-40 km)-(CE-20 km)-(2L-15 km-0°-HFLF-Cryo)	77 974	12 444	4379	396	16 827	621
LVKI-O5	49	7	0	0	10	1
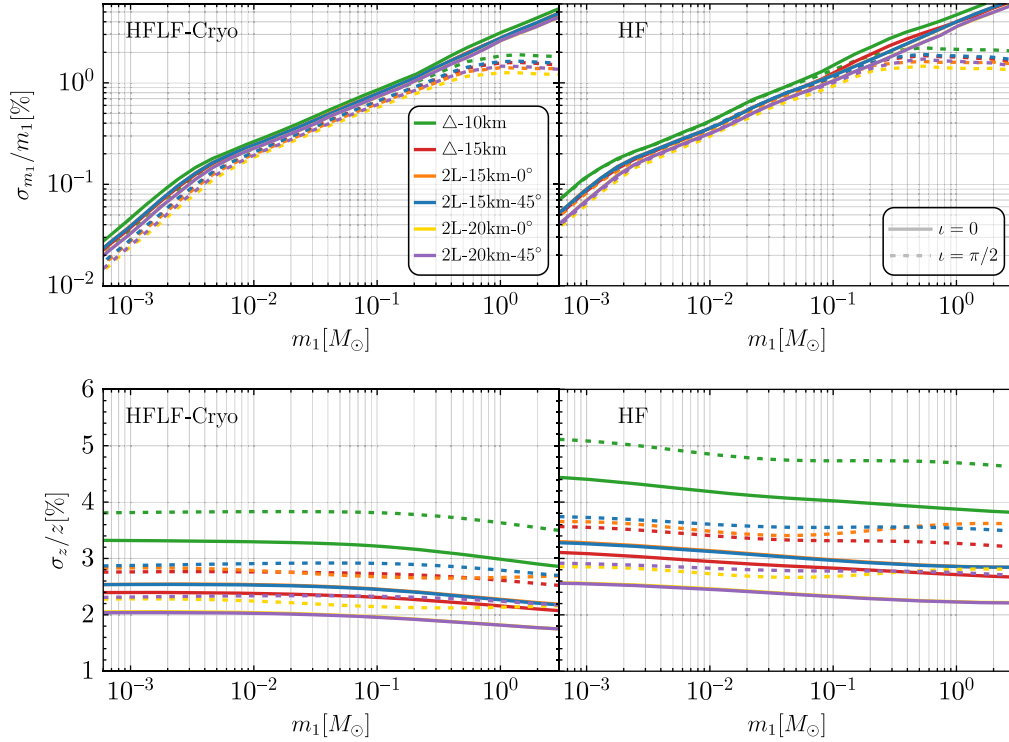
FIG. 5.   Relative error on the primary source-frame mass (top) and source redshift (bottom) as a function of m_1 in the subsolar range. We consider a source located at a distance such that the SNR = 30 in the Δ-10 km HFLF-Cryo configuration.

jeopardize the ET capability to detect subsolar-mass signatures. On the other hand, the length of the arms, which leads to a larger SNR, is mainly responsible for the different performance of the various designs.

C. Eccentricity measurements

Another key prediction of the PBH model involves the eccentricity e. As discussed in Sec. II C, while formed with large eccentricity at high redshift, PBH binaries circularize before the GW signal can enter the observation band of current and future detectors [69]. Therefore, PBH binary candidates must have small eccentricities.

To test the sensitivity of the various configurations to the measurement of a possible orbital eccentricity, we use the TaylorF2 inspiral-only waveform model [209–211] with the extension presented in Ref. [212] to account for a small eccentricity in the orbit. Using as reference values for the total source-frame mass $2M_\odot$ and $20M_\odot$, for each detector configuration, we compute the relative error that can be attained on equal-mass, nonspinning systems, as a function of the eccentricity e_0 defined at $f_{e_0} = 10$ Hz. The distance to the source is fixed to $d_L = 100$ Mpc for the case $M_{\rm tot} = 2M_\odot$ and to $d_L = 500$ Mpc for $M_{\rm tot} = 20M_\odot$.

The results for the relative errors attainable on e_0 are reported in Fig. 6. We notice, in particular, the great relevance of the LF instrument to perform eccentricity measurements, which may result in a reduction of σ_{e_0} of up to one order of magnitude. This can be traced to the

fact that eccentricity gives larger effects during the inspiral (i.e., at low frequencies), since, when going closer to merger, a binary system tends to circularize, with $e_0 \propto f_{\rm GW}^{-19/18}$. The range of values of e_0 shown on the horizontal axis in Fig. 6 corresponds to eccentricities that are too large for a PBH binary, that are expected to have $e_0 \sim 10^{-6}$ when they reach $f = 10$ Hz [69]. As a consequence, in this range, when the relative error on e_0 for a given detection is sufficiently small, e.g., below the horizontal dashed line in the figure (which corresponds to $\Delta e_0/e_0 = 0.33$), one would be able to exclude that this event has a primordial origin.

Finally, for fixed SNR, heavier mergers result in a smaller number of cycles within the ET observable frequency band and a corresponding reduction of precision (i.e., larger σ_{e_0}). As far as the comparison between configurations is concerned, we checked that analogous conclusions can be drawn from simulating detections with larger masses. A smaller improvement is brought by longer detector arms, which can amount to slightly larger SNR.

D. Tidal deformability measurements

Measurements of tidal deformability represent another crucial indicator of the compact nature of a merger. In particular, focusing on the light portion of the mass spectrum accessible to ET, tidal effects are an important discriminant between astrophysical stars (of various nature) and light PBHs.
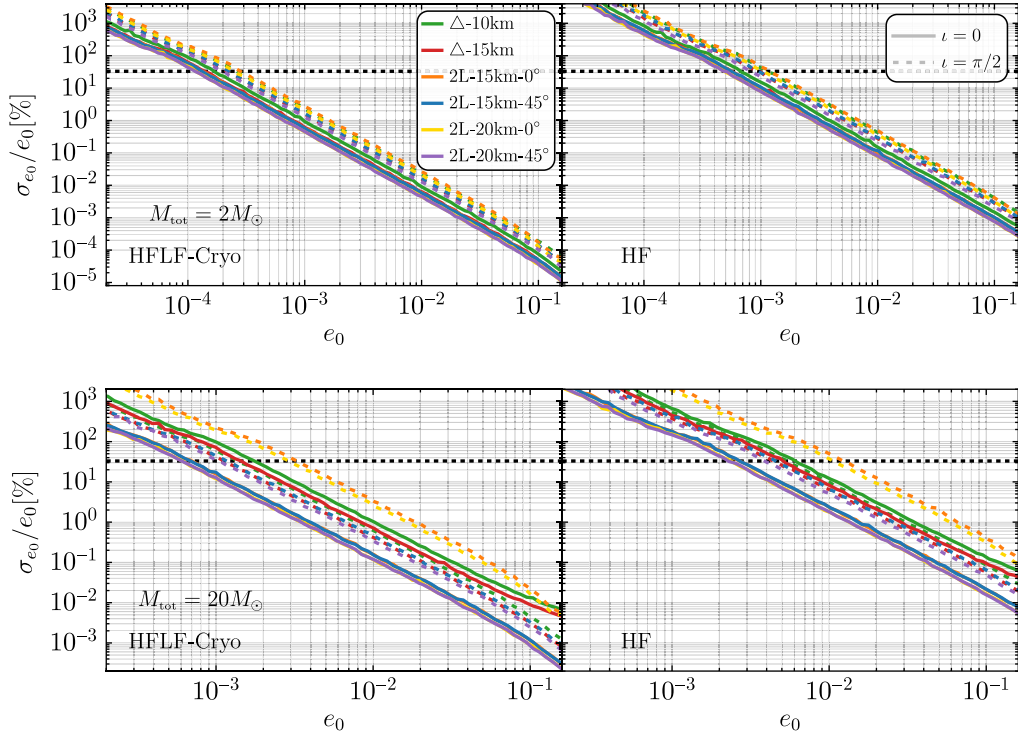
FIG. 6. Relative error on the eccentricity e_0 at $f_{e_0} = 10$ Hz as a function of its injected value for a binary with a total source-frame mass of $M_{\rm tot} = 2M_\odot$ and $d_L = 100$ Mpc in the upper panel, while $M_{\rm tot} = 20M_\odot$ and $d_L = 500$ Mpc in the lower panel. One is able to exclude negligible eccentricity (at 3σ level) below the horizontal gray dashed lines.

In Fig. 7, we show the absolute error on the tidal parameter $\tilde\Lambda$ as a function of the source-frame total mass, for nonspinning, equal-mass, and optimally oriented binaries, located at 100 Mpc from the detector, with negligible tidal deformability. The parameters we include in the FIM are

$$\{\mathcal{M}_c, \eta, d_L, \theta, \phi, \iota, \psi, t_c, \Phi_c, \chi_{1,z}, \chi_{2,z}, \tilde\Lambda, \delta\tilde\Lambda\}. \quad (14)$$

We adopt the TaylorF2 waveform model with the inclusion of tidal effects.

We also checked that, at the level of the comparison between different configurations, assuming the IMRPhenomD_NRTidalv2 waveform approximant gives analogous results. However, in the range of masses of its validity, the latter provides a smaller uncertainty on $\tilde\Lambda$, as can be seen from the dashed lines in Fig. 7. This is due to the fact that TaylorF2 describes only the inspiral part of the signal, while IMRPhenomD_NRTidalv2 is a full inspiral-merger model and includes a more complete tidal phase (recall that the tidal terms we use in TaylorF2 appear only at 5PN and 6PN order) as well as tidal terms in the amplitude (which are not present in TaylorF2). We further verified that, as a consequence of the more complete tidal phase and amplitude, even if cutting the IMRPhenomD_NRTidalv2 at $2f_{\rm ISCO}$, the uncertainty on $\tilde\Lambda$ is still more than 10 times smaller than the one estimated using TaylorF2.

Overall, the performance of the various configurations for low-mass systems is similar, with more differences appearing for higher masses, where the 2L configurations perform better compared to the triangle. We also notice the improvement thanks to the LF instrument for masses $M_{\rm tot} \gtrsim 1M_\odot$ and, in particular, for $M_{\rm tot} \gtrsim 100M_\odot$: This can be traced to the fact that a signal can stay in band for a much higher number of cycles thanks to the LF sensitivity, resulting in smaller errors on the parameters. Here again, we see that longer arms lead to slightly reduced uncertainties due to the larger expected SNR.

E. Spin measurements

As discussed in Sec. V E, in the standard formation scenario, PBH binaries composed of individual PBHs lighter than $m_{\rm PBH} \simeq 10M_\odot$ retain their initial small spins, as accretion is always not efficient enough to spin up individual components. Thus, measuring a nonvanishing spin for a sub-$10M_\odot$ object would be in tension with a standard primordial origin. Provided modeling of PBH accretion will be accurate enough, the mass-spin relation can (at least in principle) be compared with a single event to test its consistency with a primordial origin for larger masses. In order to compare the performance of various designs, in this section we forecast the accuracy with which ET could measure spins as a function of both primary mass and mass ratio, for selected individual events. In Sec. VI, we will instead show the results of a
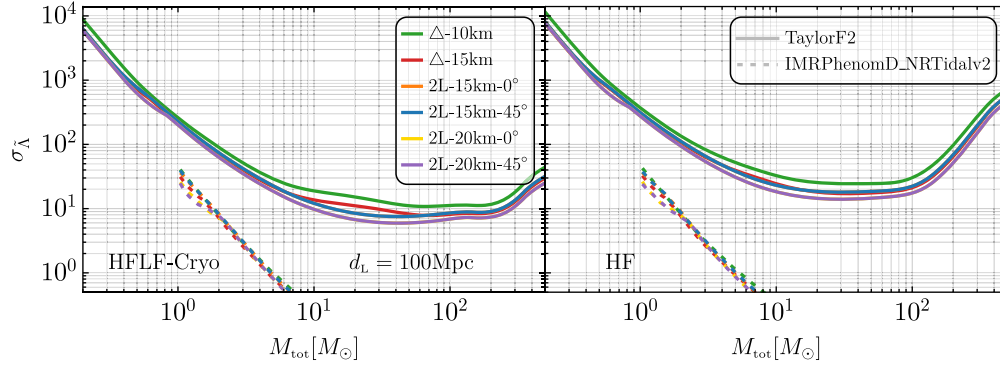
FIG. 7. Absolute (1σ) uncertainty on the tidal deformability $\tilde{\Lambda}$ as a function of total mass M_{tot} in the source frame for the various configurations. We assume negligible deformability of the source, nonspinning equal-mass binaries and an optimally oriented source at a distance of 100 Mpc. The aligned 2L configurations are not visible, as they result in comparable performance as for the misaligned case, due to our choice of selecting an optimally oriented source. We show as solid lines the results obtained over a broad mass range with the TaylorF2 inspiral-only model, while for comparison we also show the results obtained with the full inspiral-merger model IMRPhenomD_NRTidalv2 in its range of validity.

comparison based on a population analysis, which yields analogous trends.

In Fig. 8, we show the parameter space in the (m_1, q) plane in which an absolute 1σ error of $\sigma_{\chi_{i,z}} = 1\%$ ($\sigma_{\chi_{i,z}} = 5\%$) can be achieved. In this analysis, we consider vanishing spins and provide absolute errors on the spin magnitude along the angular momentum axis $\hat{z}$.

We consider a merger at a fixed distance of $d_L = 500$ Mpc. Therefore, moving toward the right-hand side (upper side) of the plot, which means larger total masses, corresponds to considering higher values of SNR. This drives an increased precision in all configurations we considered. The performance of the detectors would, of course, improve for closer sources.
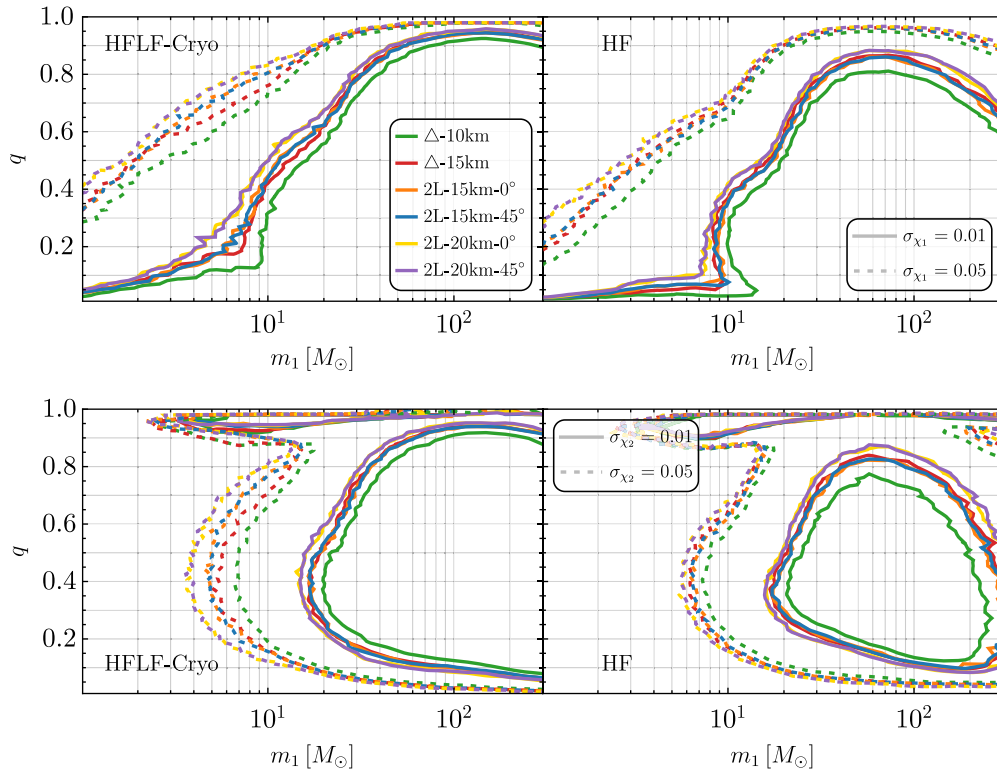

FIG. 8. Absolute errors on both primary (top panel) and secondary (bottom panel) spin magnitude. We assume a merger located at $d_L = 500$ Mpc with an optimal orientation. We also inject negligible BH spins, a value which is compatible with the primordial scenario and inefficient accretion. The errors decrease on the right of and below each contour line, mainly driven by the larger SNR.

Under the assumption of aligned spins, which we adopt to perform the FIM analysis, in the limit $q = 1$ it is difficult to make independent measurements of the individual component spins. This is because, in such a limit, the dominant terms in the waveform model are completely determined by $\chi_s \equiv (1/2)(\chi_{1,z} + \chi_{2,z})$, and the derivative with respect to the antisymmetric spin $\chi_a \equiv (1/2)(\chi_{1,z} - \chi_{2,z})$ in the Fisher information matrix is suppressed by the mass difference between the two components of the binary. Therefore, in this limit, the large uncertainty on χ_a jeopardizes our ability to constrain the individual spin magnitudes $\chi_{1,z}$ and $\chi_{2,z}$. In the opposite limit, $q \ll 1$, the error on the secondary spin magnitude increases again, due to the suppressed sensitivity on the lighter component of the binary.

As one can see, no significant difference in performance between the various configurations is observed. The main difference is brought by the length of the arms and the consequent larger SNR achieved. The region of parameter space where subpercent accuracy on $\chi_{i,z}$ is achieved is systematically smaller for the Δ-10 km, while it increases with 2L configurations and longer arms, due to the slightly larger SNR.

VI. POPULATION ANALYSIS

In this section, we analyze in detail the detection prospects of the various ET configurations with a population approach. In general, forecasts based on PBH populations must be based on underlying assumptions, given no definite evidence for their existence is available to date. In this section, we are going to assume a PBH population that saturates the upper bounds provided by current GWTC-3 [4] (and the absence of detection of subsolar-mass mergers [220,221]), as recently derived in Ref. [50]. This should be viewed as an optimistic maximum contribution from PBHs to future 3G detections and serve as a benchmark for us to compare the performance of different ET configurations.

A. PBH merger rate distribution

In the standard formation scenario that we assume throughout, the PBH merger rate at low redshift is dominated by binaries that gravitationally decouple from the Hubble flow before the matter-radiation equality [86,87]. We compute the differential volumetric PBH merger rate density following Refs. [27,31,34,80] as

$$
\frac{d\mathcal{R}_{\text{PBH}}}{dm_1 dm_2} = \frac{1.6 \times 10^6}{\text{Gpc}^3 \, \text{yr}} f_{\text{PBH}}^{53/37} \left(\frac{t(z)}{t_0}\right)^{-34/37} \left(\frac{M}{M_\odot}\right)^{-32/37}
$$
$$
\times \, \eta^{-34/37} S(M, f_{\text{PBH}}, \psi, z) \psi(m_1) \psi(m_2), \quad (15)
$$

where $\eta = m_1 m_2 / M^2$, $t_0 = 13.7$ Gyr is the current age of the Universe, and $\psi(m_i)$ is the PBH mass distribution.

The suppression factor $S < 1$ accounts for environmental effects in both the early- and late-time Universe. We can separately define each contribution as

$$
S \equiv S_{\text{early}}(M, f_{\text{PBH}}, \psi) \times S_{\text{late}}(f_{\text{PBH}}, z). \quad (16)
$$

An analytic expression for S can be found in Ref. [40], which we report here for completeness. In the early Universe, suppression results as a consequence of interactions between PBH binaries and both the surrounding dark matter inhomogeneities as well as neighboring PBHs at high redshift [23,25,27,142]. This factor takes the form

$$
S_{\text{early}} \approx 1.42 \left[\frac{\langle m^2 \rangle / \langle m \rangle^2}{\bar{N}(y) + C} + \frac{\sigma_{\text{M}}^2}{f_{\text{PBH}}^2} \right]^{-21/74} \exp[-\bar{N}], \quad (17)
$$

with

$$
\bar{N} \equiv \frac{M}{\langle m \rangle} \left(\frac{f_{\text{PBH}}}{f_{\text{PBH}} + \sigma_{\text{M}}} \right), \quad (18)
$$

and the rescaled variance of matter density perturbations takes the value $\sigma_{\text{M}} \simeq 0.004$. We also introduced the first and second momenta of the PBH average mass distribution, i.e., $\langle m \rangle$ and $\langle m^2 \rangle$, respectively. In Eq. (17), the constant factor C is defined as [see Eq. (A5) in Ref. [40]]

$$
C = \frac{f_{\text{PBH}}^2 \times \langle m^2 \rangle / (\sigma_{\text{M}} \times \langle m \rangle)^2}{\left[\frac{\Gamma(29/37)}{\sqrt{\pi}} U\left(\frac{21}{74}, \frac{1}{2}, \frac{5 f_{\text{PBH}}^2}{6 \sigma_{\text{M}}^2} \right) \right]^{-74/21} - 1}, \quad (19)
$$

where $\Gamma(x)$ is the Euler Gamma function and $U(a, b, z)$ denotes the confluent hypergeometric function.

In the late Universe, multiple encounters with other PBHs that populate small clusters formed from the initial Poisson conditions lead to a thermalization of the eccentricity distribution, which enhances the merger time and effectively reduces the late-time Universe merger rate [135,136,222–224]. By accounting for the fraction of binaries that avoid dense enough clusters and are not disrupted, one can write down this additional suppression factor as [31,40,80,225]

$$
S_{\text{late}}(x) \approx \min[1, 9.6 \times 10^{-3} x^{-0.65} \exp(0.03 \ln^2 x)], \quad (20)
$$

where we introduced the variable $x \equiv (t(z)/t_0)^{0.44} f_{\text{PBH}}$. Notice also that, for $f_{\text{PBH}} \lesssim 0.003$, one always finds $S_{\text{late}} \simeq 1$; i.e., the suppression of the merger rate due to disruption inside PBH clusters is negligible. This is also supported by the results obtained through cosmological N-body simulations finding that PBHs are essentially isolated when their abundance is small enough [79].

B. GWTC-3 upper bound

Following Ref. [50], we assume the PBH population is generated by an enhanced curvature power spectrum in
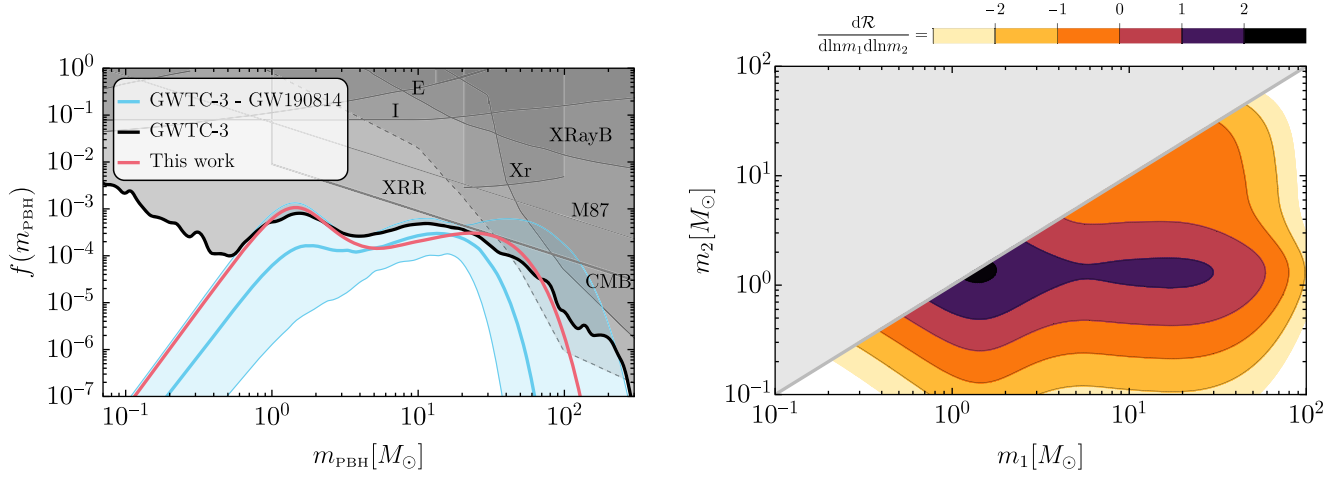
FIG. 9.   Left: constraints on the PBH mass distribution derived in Ref. [50] and compared to existing ones [16]. The thick black line delineates the GWTC-3 upper bound (90% C.I.) on PBH assuming a dominant contribution from ABH binaries and null detection of subsolar mergers. The cyan band shows the portion of the posterior where GW190814 is interpreted as a PBH binary (see Ref. [50] for more details). The red line is the mass function we consider in this work to derive optimistic detection prospects at the ET. Right: differential merger rate (in units of $\mathrm{Gpc}^{-3}\,\mathrm{yr}^{-1}$) as a function of primary and secondary mass we assume in this work.

between two scales; see Sec. II E in Ref. [50] for more details. The population is derived including a state-of-the-art modeling of the QCD era and its impact on the threshold for PBH collapse and the critical mass spectrum (see also Refs. [51,112,113,115]). Only four hyperparameters fix the PBH population: the PBH abundance f_{PBH}, the power spectrum tilt n_s (not related to the one characterizing the larger cosmic microwave background scales), and the minimum M_{S} and maximum M_{L} PBH masses, linked to the smallest and largest horizon masses bracketing the PBH formation epoch. In particular, we use $f_{\mathrm{PBH}} = 10^{-2.8}$, $n_s = 0.84$, $M_{\mathrm{S}} = 10^{-1.6} M_\odot$, and $M_{\mathrm{L}} = 10^3 M_\odot$, which corresponds to a representative upper bound on the PBH population given the currently available GWTC-3 dataset.

The red line in Fig. 9 (left panel) is the mass function that we consider in this work, alongside the most stringent constraint on this window. With this choice, the local rate density is

$$\mathcal{R}_{\mathrm{PBH}}(z = 0) = 89 \ \mathrm{Gpc}^{-3}\,\mathrm{yr}^{-1}, \qquad (21)$$

integrated over all masses in the range $m_i \in [10^{-2}, 10^3] M_\odot$. Notice, in particular, that this number is dominated by the contribution of light events, and it is smaller than what is estimated by the LVK Collaboration in the "full" mass range [5], as PBH can explain only a small fraction of current detected events [45,50]. As found in Ref. [50], the mass distribution reported in Fig. 9 (left panel, cyan band) would correspond to [0.8, 22.4] mergers in the current catalog of events at 90% CL while predicting [0.0, 0.6] events in the subsolar-mass range (compatible with zero), [0.1, 2.3] in the lower mass gap, and [0.0, 6.1] in the upper mass gap. We refer to the original paper for more details.

The intrinsic distribution of mergers in both the primary and secondary mass is shown in the right panel in Fig. 9.

The total number of mergers per year in the redshift window $z \in [0, 100]$ is

$$N_{\mathrm{PBH}}^{z \in [0,100]} = \int_0^{100} \mathrm{d}z \frac{\mathrm{d}V_c}{\mathrm{d}z} \frac{\mathcal{R}_{\mathrm{PBH}}(z)}{1 + z} = 1.92 \times 10^6/\mathrm{yr}, \quad (22)$$

which is the number of sources we analyze. We do not consider higher-redshift sources, even though they exist, as above $z = 100$ the selection bias reduces to zero the observable mergers in all configurations we considered. The sources are distributed uniformly across the sky, and we also assume uniform distributions for the inclination angle, polarization angle, phase at coalescence, and merger time.

Consistently with the above assumption of negligible effect of accretion on PBH masses adopted in Ref. [50], the spin magnitudes are drawn assuming small PBH accretion efficiency and adopting the accretion model described in detail in Refs. [34,132,226]. For definiteness, we assume a cutoff redshift $z_{\mathrm{cut-off}} 23$ *for the PBH binary accretion,* while we assume uniform and independent distributions for the spin orientations, as discussed in Sec. II B.

C. Population detection prospects at ET

We perform the analysis on the described population for all the ET configurations considered in this work, also in combination with one or two CE detectors for the full HFLF-Cryo ASD, assuming a 40 km detector in the former case and a 40 km plus a 20 km detector in the latter. As a comparison, we further perform the analysis for the LIGO-Virgo-KAGRA-LIGO India network using the most

optimistic sensitivity curves currently available for the O5 run.

The analysis is performed using the IMRPhenomXPHM waveform model for the full set of 15 parameters

$$\{\mathcal{M}_c, \eta, d_L, \theta, \phi, \theta_{JN}, \psi, t_c, \Phi_c, \chi_1, \chi_2, \theta_{s,1}, \theta_{s,2}, \phi_{JL}, \phi_{1,2}\},$$
(23)

where χ_1 and χ_2 denote the spin magnitudes of the two objects, θ_{JN} is the angle between the total angular momentum vector of the binary and the line of sight, $\theta_{s,1}$ and $\theta_{s,2}$ are the tilts of the two spins, ϕ_{JL} is the azimuthal angle of the orbital angular momentum relative to the total angular momentum, and $\phi_{1,2}$ the difference in azimuthal angle of the two spins. For each event, we compute the SNR at the various detector configuration, while the parameter estimation is performed only for the events having SNR ≥ 12.[16] To have a more realistic simulation, we assume an uncorrelated 85% duty cycle for 3G detectors (this is applied to each arm for the triangle) and a 70% duty cycle for 2G detectors during O5.

In Table I, we summarize the results for the number of detected events, imposing a conservative detection threshold SNR ≥ 12, which is the same adopted for the parameter estimation. In particular, in the second column, we report the results for the total number of observed events.[17]

Furthermore, following the logic described in Ref. [50], we report the number of detections per year falling in "special" mass ranges, which would somehow challenge vanilla astrophysical scenarios. These are of particular interest, since the astrophysical mechanisms producing BHs with such masses are poorly understood, and PBHs offer a natural alternative. In particular, in the third column, we restrict to the systems having at least one of the masses lighter than $1M_\odot$ (with our convention $m_1 \geq m_2$, this condition is equivalent to $m_2 \leq 1M_\odot$). In the fourth (fifth) column instead, we report the number of observations of events at redshift $z \geq 10$ ($z \geq 30$). Finally, in the sixth column, we report the number of observed sources having at least one of the objects with a mass falling in the so-called lower mass gap (LMG), i.e., in the range $[2.5, 5]M_\odot$, while in the seventh column the ones having at least one object with a mass falling in the upper mass gap (UMG), i.e., above $50M_\odot$ (this condition is equivalent to

$m_1 \geq 50M_\odot$). In the top rows in Table I, we also report the number of mergers produced by the intrinsic population per year (i.e., before the selection bias of the detector is applied). This helps gain intuition on how restrictive is the limited sensitivity of the detector within the various range of the mass-distance parameter space.

Already from these results, a number of conclusions can be drawn: Comparing the HFLF-Cryo and HF results, we see the fundamental importance of the LF instrument in the ET design, which enables one to observe binaries up to extremely high redshifts, one of the strong signatures of PBHs, while also more than doubling the number of overall detections. We further notice the overall better results obtained with the 2L-15 km configuration as compared to the 10 km triangular geometry. Given that the adopted population predicts a high number of binaries with low masses (around $1M_\odot$ and $2M_\odot$ as can be seen from Fig. 9), we also appreciate the performance of the CE detectors, which are more sensitive than ET for such events (see, e.g., Fig. 4 in Ref. [64]), but still notice the significant improvement brought by ET, showing the potential of the full 3G network. Finally, comparing the results obtained for 3G detectors to the ones for the LVKI O5 network, we see the huge leap achievable thanks to ET and CE.

The overall conclusion we draw from these findings is that 3G detectors will be able to discover a PBH population which may be undetected by current experiments. Both the subsolar and high-redshift smoking-gun signatures would provide unique probes of the existence of such population, with the latter being accessible only if the HFLF-Cryo ET configuration is achieved. In both mass gaps, the number of detectable events can reach multiple thousands, which would further allow one to perform dedicated population analyses aimed at distinguishing these contributions from astrophysical contaminants in those regions. In case such events were not discovered, ET would set much more stringent bounds on the abundance of PBHs in the stellar mass range than what can optimistically achieved with current LIGO, Virgo, and KAGRA detector technology [65].

In Fig. 10, we show the distribution of mergers as a function of redshift z. Because of the small rates, large search volumes are needed in order to obtain a sizable number of events. This means that most of the detectable mergers fall in the redshift range between $z \approx \mathcal{O}(0.1)$ and $z \approx \mathcal{O}(40)$, with the latter boundary of this range which strongly depends on the specific design considered. While the black line shows the full population for reference, the colored solid and dashed lines correspond to the histogram of events detected with SNR larger than 12 or 50, respectively. This plot graphically shows that the HF version of the design is not able to reach mergers beyond redshift $\mathcal{O}(30)$, not even in the largest (2L-20 km) implementation, thus missing entirely the high-redshift (smoking-gun) window. On the other hand, the difference between HF and HFLF-Cryo is reduced in the bulk of

---

[16]We further discard a small fraction of events having an ill-conditioned Fisher matrix, which is found never to exceed 1%. See Ref. [64] for a discussion of the methodology.

[17]Real world search pipelines are based on more advanced statistics, such as the false-alarm rate. However, this requires a detailed understanding of the level of non-Gaussian noise in the detector, which can be obtained only after a detector has been built and commissioned. Nevertheless, we expect the SNR criterion to allow for a consistent comparison between configurations, as well as a reliable estimate of the performance of the detectors.
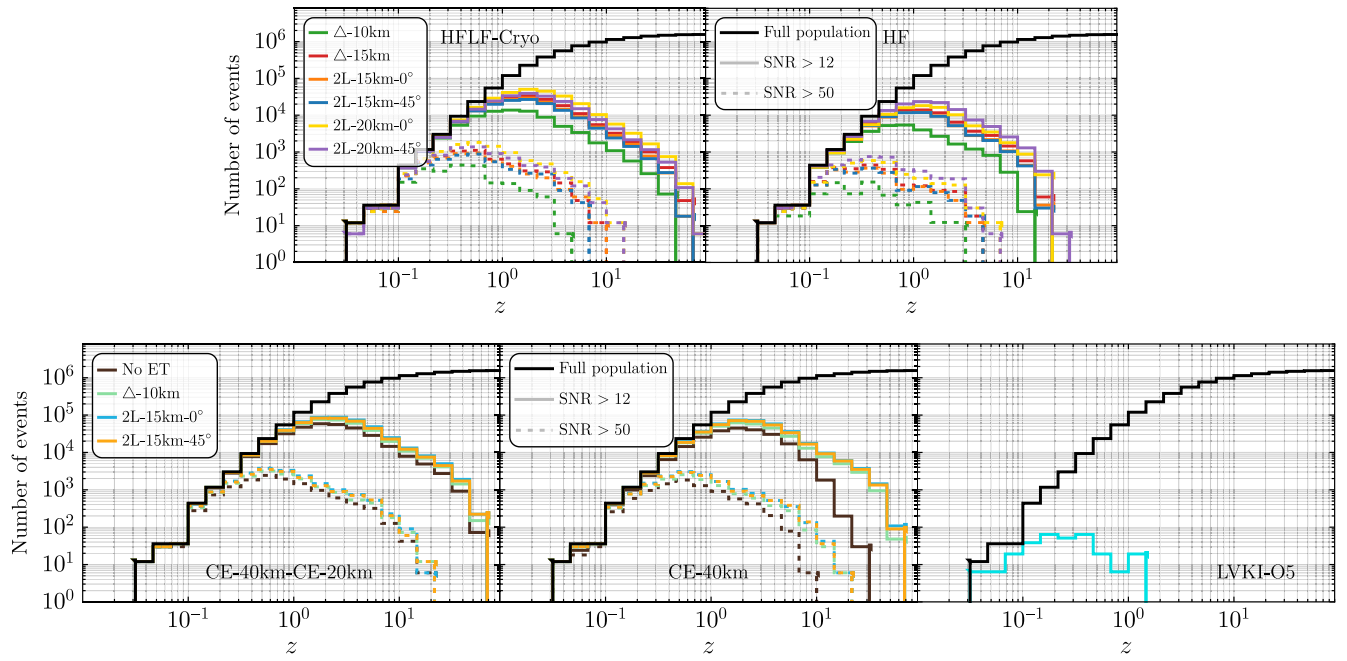
FIG. 10. Probability density function of detected events (with SNR > 12 and SNR > 50) for the population assumed in Sec. VI B. The black solid line indicates the entire population of mergers per year. The number of detections per bin is monotonically increasing, as we choose a binning equally spaced in log scale. In practice, the event distribution in redshift follows the integrand in Eq. (22), which peaks at redshift $z \approx \mathcal{O}(10)$ because of the comoving volume factor.
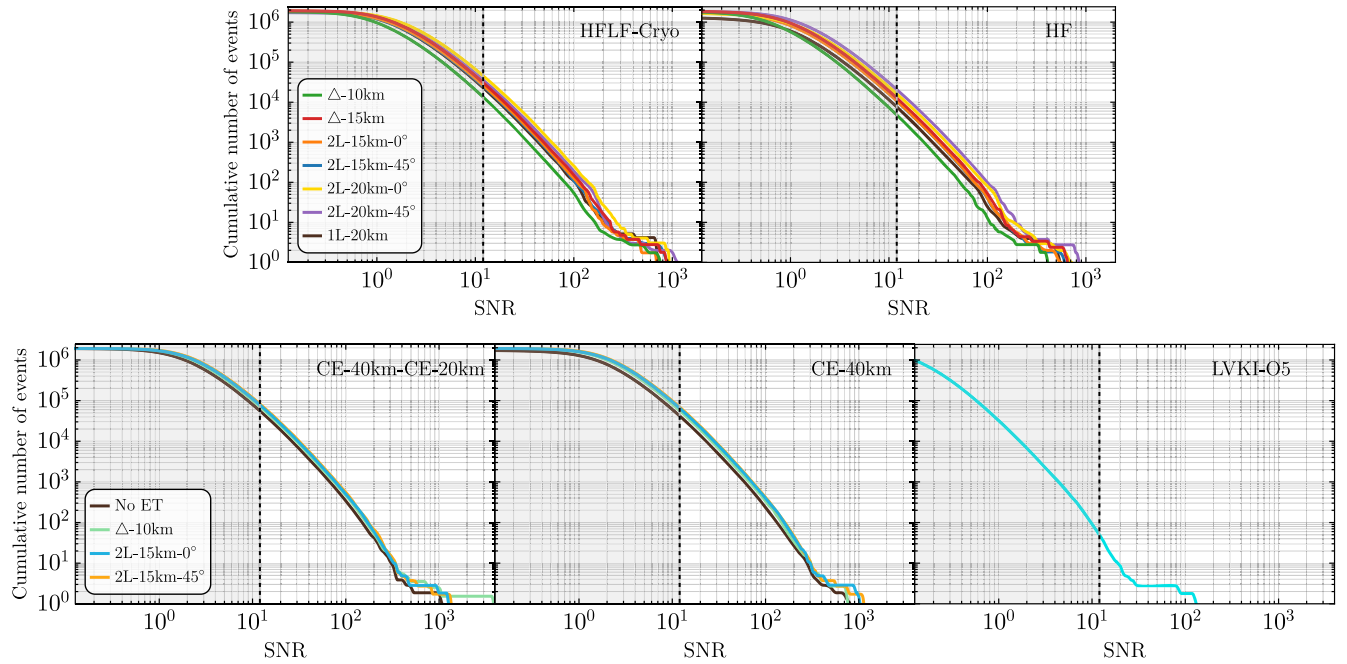

FIG. 11. Cumulative distribution of the SNRs for the simulated PBH population as observed by the different detector configurations. The cumulative is inverted to actually show the number of events with a SNR higher than a given value, and we shade the region SNR < 12, which is below the assumed detection threshold. Top panel: configurations featuring only the ET detector geometries considered with their HFLF-Cryo sensitivity (left panel) and HF sensitivity (right panel). Bottom panel: network of detectors which features either two CE (with and without ET) and, on the rightmost side, the optimistic O5 LIGO-Virgo-KAGRA-LIGO India detector performance.
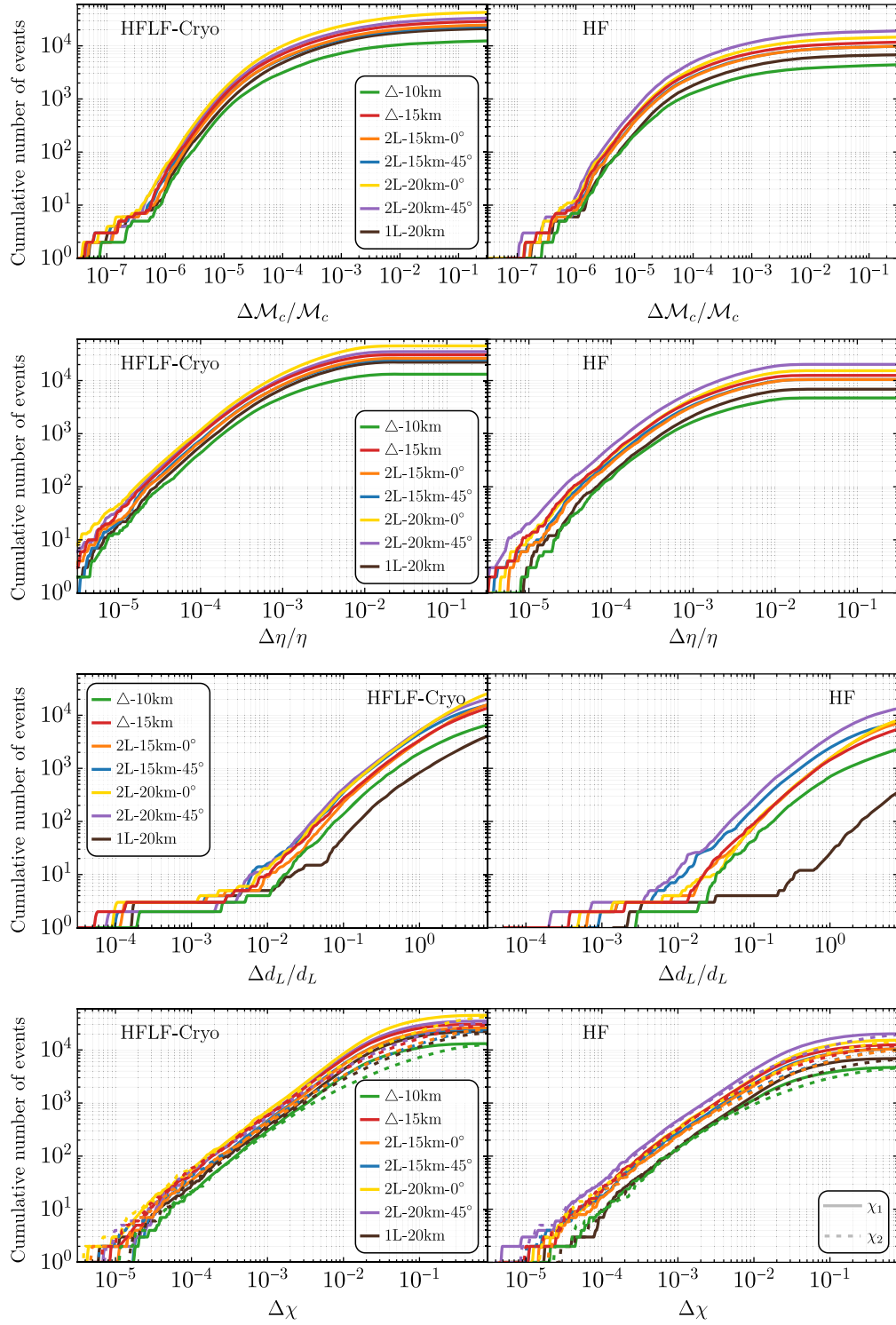
FIG. 12. Cumulative distribution of parameter estimation errors for some selected parameters obtained with the Fisher matrix approach for the simulated PBH population as observed by the different detector geometries considered with their HFLF-Cryo sensitivity (left panel) and HF sensitivity (right panel). In particular, in the top row we report the relative errors attainable on the detector-frame chirp mass, in the second row for the symmetric mass ratio, and in the third row on the luminosity distance, while in the bottom row we report the absolute errors attainable on the adimensional spin magnitude of the primary (solid line) and secondary (dashed line) object.

events, as similar numbers are obtained below redshifts of a few, where all designs have an outstanding performance.

Anyway, a note of caution is needed here. The sole fact that a merger happening at $z \gtrsim 30$ is detectable does not assure a good reconstruction of its distance. As already discussed in the preceding section, individual merger detections require sufficient precision on the source

redshift in order to prove the primordial nature of the source (see Refs. [109,111] for an in-depth analysis of this parameter estimation uncertainties based on Bayesian PE and Ref. [219] for figures of merit describing the attainable lower confidence level on the redshift). One could also exploit a population-based inference of the high-redshift merger rate. In such a way, multiple event detections can be
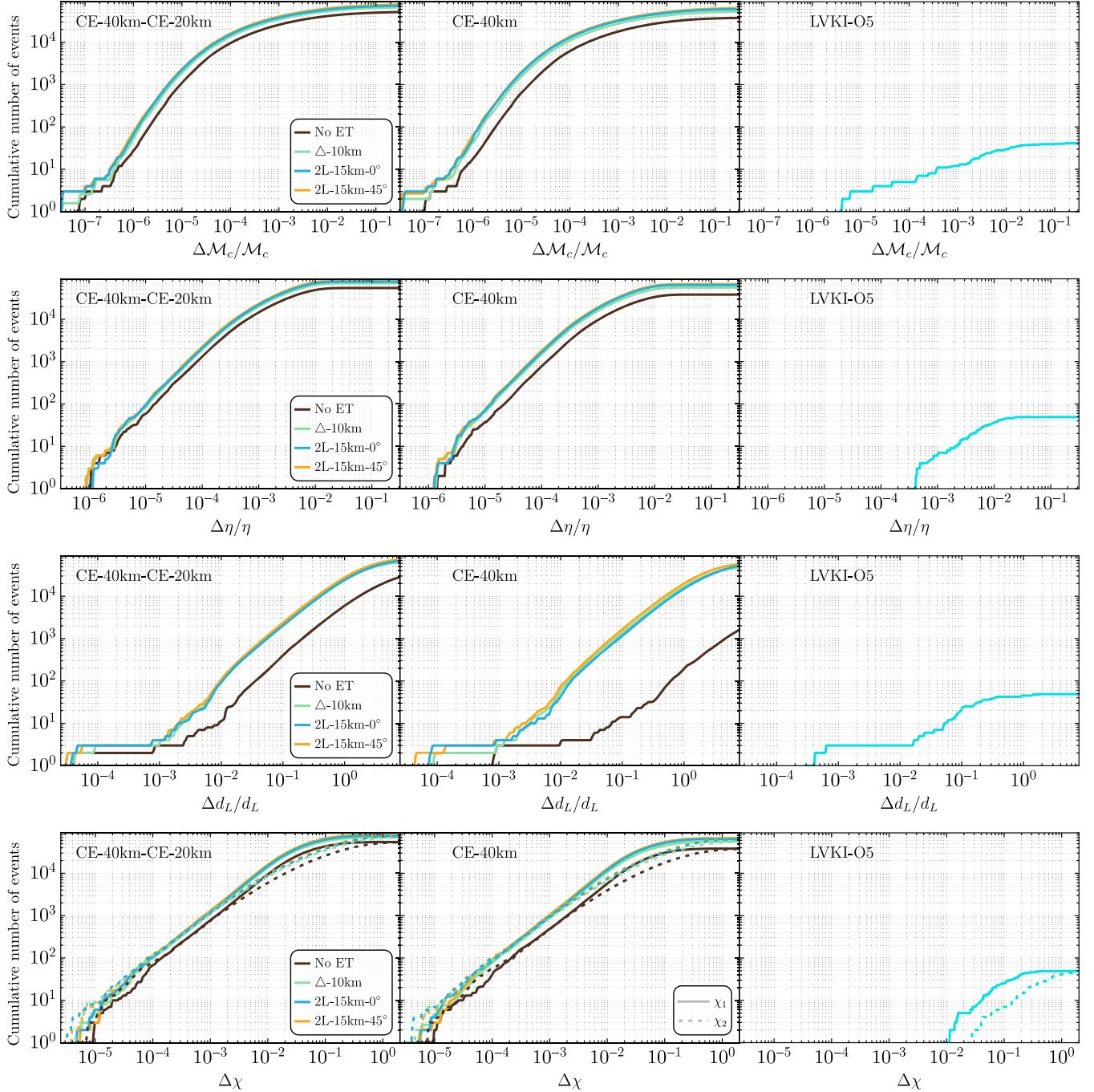
FIG. 13. The same as Fig. 12, but networks which include two CE detectors, one 40 km long and the other 20 km long (left panels), or a single 40 km CE detector (central panel) alone and in a network with the ET both in its 10 km triangular design and in the 15 km 2L designs aligned and misaligned, all with their HFLF-Cryo sensitivity. In the right panels, we report the results obtained for the optimistic version of LVKI network with the best sensitivities representative of the O5 run.

combined, thus enhancing the statistics and reducing the overall uncertainties [70,110]. In any case, this simplified comparison solidly shows the importance of the cryogenic instrument in order to access the high-redshift smoking-gun signature.

We report in Fig. 11 (top panel) the cumulative distributions of SNRs attainable at ET with all the considered geometries and the two ASDs, while in the bottom panels we show the same results for CE (both as a single 40 km detector and as two instruments of 40 and 20 km) both alone and in a network with ET and for the LVKI network during the O5 observing run.

In Figs. 12 and 13, we report the cumulative distribution of parameter estimation errors on the most relevant parameters characterizing each event in the population of PBHs.

As far as ET alone is concerned, we again notice the overall better results obtained with the 2L misaligned instruments, especially in the HF scenario, both for the measurement of the intrinsic parameters and, in particular, for the luminosity distance reconstruction. Moreover, we again confirm the relevance of the LF instrument, with a number of detections more than 2 times higher as compared to the HF case, and more events having good parameter reconstruction. Considering ET in a network with CE, the differences among the three considered geometries appear instead less pronounced, with the 2L configurations providing anyway better results.

VII. SUMMARY AND CONCLUSIONS

In this paper, we have analyzed how different detector designs for the ET would perform on the estimation and discrimination of some key observables of PBH mergers, as well as their detection prospects for a realistic population of PBH events [50]. In particular, we have studied three detector geometries: a triangular detector consisting of three nested instruments and two L-shaped detectors, both parallel and misaligned by 45° among them. For the various geometries, we have further considered two different arm lengths and two scenarios: one in which the detectors operate at their full potential and adopt a xylophone design, i.e., consist of two instruments, one optimized for LF sensitivity and the other for HF sensitivity, and another in which only the HF instrument is operating. For a comprehensive analysis of how other science cases depend on these configurations, we refer to Ref. [72], where also the results here presented are summarized.

Overall, we find that, thanks to the improved sensitivity and the wider bandwidth, 3G detectors are much more likely to detect mergers of PBH binaries as compared to current facilities (mainly due to the extended reach) and have the potential to measure their parameters with sufficient accuracy to distinguish them from the astrophysical BHs. These observables include, in particular, (i) the masses in the subsolar window (where ABHs are not

expected to form); (ii) the distance in the high-z window for PBHs of mass around few tens of solar mass (after $z \gtrsim 30$ astrophysical BH are not expected to exist); and (iii) the spins (which are relevant due to the expected mass-spin correlation for PBH). This can possibly shed light on the possible primordial origin of some binaries, even on a single-event basis. This is also supported by the comparison of the results attainable at ET with the ones for the LVKI network during O5 (reported in the context of the population analysis in Figs. 12 and 13); we see how big is the leap from 2G to 3G instruments, giving a hint of how deeply instruments such as ET will enable us to look in the window 2G detectors opened on our Universe.

One of the key results emerging from our analyses is the relevance of the low-frequency instrument for PBH observations: Losing the LF sensitivity would dramatically reduce the redshift range, as is apparent from Figs. 2 and 4, at the level of potentially inhibiting the observation of mergers above $z \approx 30$, one of the smoking-gun signatures of PBH binaries and an extremely interesting region of our Universe to explore. The LF instrument turns out to be fundamental also for measuring a possible orbital eccentricity (PBH binaries are expected to have almost circular orbits) and enables one to detect more than twice the number of events as compared to the HF case looking at the population analysis, also resulting in tighter parameter errors, irrespectively of the geometry.

We further find the longer detectors to be preferable, as expected, in particular, for the observable range and the number of detections, as well as for parameter estimation. Concerning the detector geometry, we find the 2L configuration with misaligned arms to provide the best option. In particular, it provides a better estimation performance on all the parameters and enables one to observe a higher number of events as compared to the triangular design [we are here comparing the 2L design with 15 km (20 km) arms and the triangular design with 10 km (15 km) arms].[18] When considering ET in a network with CE, the differences among the various detector geometries are smaller, as can be seen from the population analysis results, with the 2L configurations still being preferred.

ACKNOWLEDGMENTS

---

[18]What will be the most appropriate comparison between the arm length of the triangle and 2L configurations can be ascertained only with a detailed analysis of the relative costs (as well as, possibly, of the different funding schemes), currently under development within the ET Collaboration.

[1] B. P. Abbott *et al.* (LIGO Scientific and Virgo Collaborations), Phys. Rev. Lett. **116**, 061102 (2016).

[2] B. P. Abbott *et al.* (LIGO Scientific and Virgo Collaborations), Phys. Rev. X **9**, 031040 (2019).

[3] R. Abbott *et al.* (LIGO Scientific and Virgo Collaborations), Phys. Rev. X **11**, 021053 (2021).

[4] R. Abbott *et al.* (LIGO Scientific, Virgo, and KAGRA Collaborations), arXiv:2111.03606 [Phys. Rev. X (to be published)].

[5] R. Abbott *et al.* (KAGRA, Virgo, and LIGO Scientific Collaborations), Phys. Rev. X **13**, 011048 (2023).

[6] S. Vitale, Science **372**, abc7397 (2021).

[7] I. Mandel and F. S. Broekgaarden, Living Rev. Relativity **25**, 1 (2022).

[8] Y. B. Zel'dovich and I. D. Novikov, Sov. Astron. AJ (Engl. Transl.), **10**, 602 (1967), https://ui.adsabs.harvard.edu/abs/1967SvA....10..602Z/abstract.

[9] S. W. Hawking, Nature (London) **248**, 30 (1974).

[10] G. F. Chapline, Nature (London) **253**, 251 (1975).

[11] B. J. Carr, Astrophys. J. **201**, 1 (1975).

[12] P. Ivanov, P. Naselsky, and I. Novikov, Phys. Rev. D **50**, 7173 (1994).

[13] J. Garcia-Bellido, A. D. Linde, and D. Wands, Phys. Rev. D **54**, 6040 (1996).

[14] P. Ivanov, Phys. Rev. D **57**, 7145 (1998).

[15] S. Blinnikov, A. Dolgov, N. K. Porayko, and K. Postnov, J. Cosmol. Astropart. Phys. 11 (2016) 036.

[16] B. Carr, K. Kohri, Y. Sendouda, and J. Yokoyama, Rep. Prog. Phys. **84**, 116902 (2021).

[17] M. Volonteri, Astron. Astrophys. Rev. **18**, 279 (2010).

[18] S. Clesse and J. García-Bellido, Phys. Rev. D **92**, 023524 (2015).

[19] P. D. Serpico, V. Poulin, D. Inman, and K. Kohri, Phys. Rev. Res. **2**, 023204 (2020).

[20] S. Bird, I. Cholis, J. B. Muñoz, Y. Ali-Haïmoud, M. Kamionkowski, E. D. Kovetz, A. Raccanelli, and A. G. Riess, Phys. Rev. Lett. **116**, 201301 (2016).

[21] S. Clesse and J. García-Bellido, Phys. Dark Universe **15**, 142 (2017).

[22] M. Sasaki, T. Suyama, T. Tanaka, and S. Yokoyama, Phys. Rev. Lett. **117**, 061101 (2016); **121**, 059901(E) (2018).

[23] Y. N. Eroshenko, J. Phys. Conf. Ser. **1051**, 012010 (2018).

[24] S. Wang, Y.-F. Wang, Q.-G. Huang, and T. G. F. Li, Phys. Rev. Lett. **120**, 191102 (2018).

[25] Y. Ali-Haïmoud, E. D. Kovetz, and M. Kamionkowski, Phys. Rev. D **96**, 123523 (2017).

[26] Z.-C. Chen and Q.-G. Huang, Astrophys. J. **864**, 61 (2018).

[27] M. Raidal, C. Spethmann, V. Vaskonen, and H. Veermäe, J. Cosmol. Astropart. Phys. 02 (2019) 018.

[28] S. Wang, T. Terada, and K. Kohri, Phys. Rev. D **99**, 103531 (2019); **101**, 069901(E) (2020).

[29] L. Liu, Z.-K. Guo, and R.-G. Cai, Eur. Phys. J. C **79**, 717 (2019).

[30] G. Hütsi, M. Raidal, and H. Veermäe, Phys. Rev. D **100**, 083016 (2019).

[31] V. Vaskonen and H. Veermäe, Phys. Rev. D **101**, 043015 (2020).

[32] A. D. Gow, C. T. Byrnes, A. Hall, and J. A. Peacock, J. Cosmol. Astropart. Phys. 01 (2020) 031.

[33] Y. Wu, Phys. Rev. D **101**, 083008 (2020).

[34] V. De Luca, G. Franciolini, P. Pani, and A. Riotto, J. Cosmol. Astropart. Phys. 06 (2020) 044.

[35] A. Hall, A. D. Gow, and C. T. Byrnes, Phys. Rev. D **102**, 123524 (2020).

[36] S. Bhagwat, V. De Luca, G. Franciolini, P. Pani, and A. Riotto, J. Cosmol. Astropart. Phys. 01 (2021) 037.

[37] V. De Luca, V. Desjacques, G. Franciolini, P. Pani, and A. Riotto, Phys. Rev. Lett. **126**, 051101 (2021).

[38] J. García-Bellido, J. F. Nuño Siles, and E. Ruiz Morales, Phys. Dark Universe **31**, 100791 (2021).

[39] K. W. K. Wong, G. Franciolini, V. De Luca, V. Baibhav, E. Berti, P. Pani, and A. Riotto, Phys. Rev. D **103**, 023026 (2021).

[40] G. Hütsi, M. Raidal, V. Vaskonen, and H. Veermäe, J. Cosmol. Astropart. Phys. 03 (2021) 068.

[41] K. Kritos, V. De Luca, G. Franciolini, A. Kehagias, and A. Riotto, J. Cosmol. Astropart. Phys. 05 (2021) 039.

[42] V. De Luca, G. Franciolini, P. Pani, and A. Riotto, J. Cosmol. Astropart. Phys. 05 (2021) 003.

[43] H. Deng, J. Cosmol. Astropart. Phys. 04 (2021) 058.

[44] R. Kimura, T. Suyama, M. Yamaguchi, and Y.-L. Zhang, J. Cosmol. Astropart. Phys. 04 (2021) 031.

[45] G. Franciolini, V. Baibhav, V. De Luca, K. K. Y. Ng, K. W. K. Wong, E. Berti, P. Pani, A. Riotto, and S. Vitale, Phys. Rev. D **105**, 083526 (2022).

[46] S. S. Bavera, G. Franciolini, G. Cusin, A. Riotto, M. Zevin, and T. Fragos, Astron. Astrophys. **660**, A26 (2022).

[47] L. Liu, X.-Y. Yang, Z.-K. Guo, and R.-G. Cai, J. Cosmol. Astropart. Phys. 01 (2023) 006.

[48] X. Wang, Y.-l. Zhang, R. Kimura, and M. Yamaguchi, Sci. China Phys. Mech. Astron. **66**, 260462 (2023).

[49] L.-M. Zheng, Z. Li, Z.-C. Chen, H. Zhou, and Z.-H. Zhu, Phys. Lett. B **838**, 137720 (2023).

[50] G. Franciolini, I. Musco, P. Pani, and A. Urbano, Phys. Rev. D **106**, 123526 (2022).

[51] A. Escrivà, E. Bagui, and S. Clesse, J. Cosmol. Astropart. Phys. 05 (2023) 004.

[52] M. Sasaki, T. Suyama, T. Tanaka, and S. Yokoyama, Classical Quantum Gravity **35**, 063001 (2018).

[53] A. M. Green and B. J. Kavanagh, J. Phys. G **48**, 4 (2021).

[54] G. Franciolini, Primordial black holes: From theory to gravitational wave observations, Ph.D. thesis, Geneva Uninversity, Department of Theoretical Physics, 2021.

[55] S. Hild, S. Chelkowski, and A. Freise, arXiv:0810.0604.

[56] M. Punturo et al., Classical Quantum Gravity **27**, 194002 (2010).

[57] S. Hild et al., Classical Quantum Gravity **28**, 094013 (2011).

[58] D. Reitze et al., Bull. Am. Astron. Soc. **51**, 035 (2019), https://ui.adsabs.harvard.edu/abs/2019BAAS...51g..35R/abstract.

[59] M. Evans et al., arXiv:2109.09882.

[60] P. Amaro-Seoane, H. Audley, S. Babak et al., arXiv:1702.00786.

[61] M. Maggiore et al., J. Cosmol. Astropart. Phys. 03 (2020) 050.

[62] V. Kalogera et al., arXiv:2111.06990.

[63] S. Borhanian and B. S. Sathyaprakash, arXiv:2202.11048.

[64] F. Iacovelli, M. Mancarella, S. Foffa, and M. Maggiore, Astrophys. J. **941**, 208 (2022).

[65] V. De Luca, G. Franciolini, P. Pani, and A. Riotto, J. Cosmol. Astropart. Phys. 11 (2021) 039.

[66] O. Pujolas, V. Vaskonen, and H. Veermäe, Phys. Rev. D **104**, 083521 (2021).

[67] S. Mukherjee, M. S. P. Meinema, and J. Silk, Mon. Not. R. Astron. Soc. **510**, 6218 (2022).

[68] S. Mukherjee and J. Silk, Mon. Not. R. Astron. Soc. **506**, 3977 (2021).

[69] G. Franciolini, R. Cotesta, N. Loutrel, E. Berti, P. Pani, and A. Riotto, Phys. Rev. D **105**, 063510 (2022).

[70] K. K. Y. Ng, G. Franciolini, E. Berti, P. Pani, A. Riotto, and S. Vitale, Astrophys. J. Lett. **933**, L41 (2022).

[71] https://www.et-gw.eu/index.php/observational-science-board.

[72] M. Branchesi, M. Maggiore et al., arXiv:2303.15923.

[73] V. De Luca, V. Desjacques, G. Franciolini, A. Malhotra, and A. Riotto, J. Cosmol. Astropart. Phys. 05 (2019) 018.

[74] M. Mirbabayi, A. Gruzinov, and J. Noreña, J. Cosmol. Astropart. Phys. 03 (2020) 017.

[75] Y. Ali-Haïmoud, Phys. Rev. Lett. **121**, 081304 (2018).

[76] V. Desjacques and A. Riotto, Phys. Rev. D **98**, 123533 (2018).

[77] G. Ballesteros, P. D. Serpico, and M. Taoso, J. Cosmol. Astropart. Phys. 10 (2018) 043.

[78] A. Moradinezhad Dizgah, G. Franciolini, and A. Riotto, J. Cosmol. Astropart. Phys. 11 (2019) 001.

[79] D. Inman and Y. Ali-Haïmoud, Phys. Rev. D **100**, 083528 (2019).

[80] V. De Luca, V. Desjacques, G. Franciolini, and A. Riotto, J. Cosmol. Astropart. Phys. 11 (2020) 028.

[81] T. Harada, C.-M. Yoo, K. Kohri, and K.-I. Nakao, Phys. Rev. D **96**, 083517 (2017); **99**, 069904(E) (2019).

[82] M. M. Flores and A. Kusenko, Phys. Rev. D **104**, 063008 (2021).

[83] G. Dvali, F. Kühnel, and M. Zantedeschi, Phys. Rev. D **104**, 123507 (2021).

[84] Y. N. Eroshenko, J. Cosmol. Astropart. Phys. 12 (2021) 041.

[85] V. De Luca, G. Franciolini, A. Kehagias, P. Pani, and A. Riotto, Phys. Lett. B **832**, 137265 (2022).

[86] T. Nakamura, M. Sasaki, T. Tanaka, and K. S. Thorne, Astrophys. J. Lett. **487**, L139 (1997).

[87] K. Ioka, T. Chiba, T. Tanaka, and T. Nakamura, Phys. Rev. D **58**, 063003 (1998).

[88] K. Kritos, V. Strokov, V. Baibhav, and E. Berti, arXiv:2210.10055.

[89] M. Raidal, V. Vaskonen, and H. Veermäe, J. Cosmol. Astropart. Phys. 09 (2017) 037.

[90] S. M. Koushiappas and A. Loeb, Phys. Rev. Lett. **119**, 221104 (2017).

[91] R. Schneider, A. Ferrara, B. Ciardi, V. Ferrari, and S. Matarrese, Mon. Not. R. Astron. Soc. **317**, 385 (2000).

[92] R. Schneider, A. Ferrara, P. Natarajan, and K. Omukai, Astrophys. J. **571**, 30 (2002).

[93] R. Schneider, A. Ferrara, R. Salvaterra, K. Omukai, and V. Bromm, Nature (London) **422**, 869 (2003).

[94] V. Bromm, Astrophys. J. **642**, 382 (2006).

[95] R. S. de Souza, N. Yoshida, and K. Ioka, Astron. Astrophys. **533**, A32 (2011).

[96] P. Mocz et al., Mon. Not. R. Astron. Soc. **494**, 2027 (2020).

[97] B. Liu and V. Bromm, Mon. Not. R. Astron. Soc. **495**, 2475 (2020).

[98] M. Trenti and M. Stiavelli, Astrophys. J. **694**, 879 (2009).

[99] L. Tornatore, S. Borgani, K. Dolag, and F. Matteucci, Mon. Not. R. Astron. Soc. **382**, 1050 (2007).

[100] T. Kinugawa, K. Inayoshi, K. Hotokezaka, D. Nakauchi, and T. Nakamura, Mon. Not. R. Astron. Soc. **442**, 2963 (2014).

[101] T. Kinugawa, A. Miyamoto, N. Kanda, and T. Nakamura, Mon. Not. R. Astron. Soc. **456**, 1093 (2016).

[102] T. Hartwig, M. Volonteri, V. Bromm, R. S. Klessen, E. Barausse, M. Magg, and A. Stacy, Mon. Not. R. Astron. Soc. **460**, L74 (2016).

[103] K. Belczynski, T. Ryu, R. Perna, E. Berti, T. L. Tanaka, and T. Bulik, Mon. Not. R. Astron. Soc. **471**, 4702 (2017).

[104] K. Inayoshi, R. Hirai, T. Kinugawa, and K. Hotokezaka, Mon. Not. R. Astron. Soc. **468**, 5020 (2017).

[105] B. Liu and V. Bromm, Astrophys. J. Lett. **903**, L40 (2020).

[106] T. Kinugawa, T. Nakamura, and H. Nakano, Mon. Not. R. Astron. Soc. **498**, 3946 (2020).

[107] A. Tanikawa, H. Susa, T. Yoshida, A. A. Trani, and T. Kinugawa, Astrophys. J. **910**, 30 (2021).

[108] N. Singh, T. Bulik, K. Belczynski, and A. Askar, Astron. Astrophys. **667**, A2 (2022).

[109] K. K. Y. Ng, S. Chen, B. Goncharov, U. Dupletsa, S. Borhanian, M. Branchesi, J. Harms, M. Maggiore, B. S. Sathyaprakash, and S. Vitale, Astrophys. J. Lett. **931,** L12 (2022).

[110] M. Martinelli, F. Scarcella, N. B. Hogg, B. J. Kavanagh, D. Gaggero, and P. Fleury, J. Cosmol. Astropart. Phys. 08 (2022) 006.

[111] K. K. Y. Ng *et al.*, Phys. Rev. D **107,** 024041 (2023).

[112] K. Jedamzik, Phys. Rev. D **55,** R5871 (1997).

[113] C. T. Byrnes, M. Hindmarsh, S. Young, and M. R. S. Hawkins, J. Cosmol. Astropart. Phys. 08 (2018) 041.

[114] B. Carr, S. Clesse, J. García-Bellido, and F. Kühnel, Phys. Dark Universe **31,** 100755 (2021).

[115] I. Musco, K. Jedamzik, and S. Young, arXiv:2303.07980.

[116] S. Clesse and J. Garcia-Bellido, Phys. Dark Universe **38,** 101111 (2022).

[117] S. Shandera, D. Jeong, and H. S. G. Gebhardt, Phys. Rev. Lett. **120,** 241102 (2018).

[118] V. Cardoso and P. Pani, Living Rev. Relativity **22,** 4 (2019).

[119] H.-K. Guo, K. Sinha, and C. Sun, J. Cosmol. Astropart. Phys. 09 (2019) 032.

[120] J. Bramante, T. Linden, and Y.-D. Tsai, Phys. Rev. D **97,** 055016 (2018).

[121] R. Garani, Y. Genolini, and T. Hambye, J. Cosmol. Astropart. Phys. 05 (2019) 035.

[122] V. Takhistov, G. M. Fuller, and A. Kusenko, Phys. Rev. Lett. **126,** 071101 (2021).

[123] B. Dasgupta, R. Laha, and A. Ray, Phys. Rev. Lett. **126,** 141105 (2021).

[124] P. Giffin, J. Lloyd, S. D. McDermott, and S. Profumo, Phys. Rev. D **105,** 123030 (2022).

[125] R. Garani, D. Levkov, and P. Tinyakov, Phys. Rev. D **105,** 063019 (2022).

[126] D. Singh, A. Gupta, E. Berti, S. Reddy, and B. S. Sathyaprakash, Phys. Rev. D **107,** 083037 (2023).

[127] S. Bhattacharya, B. Dasgupta, R. Laha, and A. Ray, arXiv:2302.07898.

[128] M. Abramowicz, M. Bejger, A. Udalski, and M. Wielgus, Astrophys. J. Lett. **935,** L28 (2022).

[129] M. Fasano, K. W. K. Wong, A. Maselli, E. Berti, V. Ferrari, and B. S. Sathyaprakash, Phys. Rev. D **102,** 023025 (2020).

[130] F. Hofmann, E. Barausse, and L. Rezzolla, Astrophys. J. Lett. **825,** L19 (2016).

[131] J. M. Bardeen, J. Bond, N. Kaiser, and A. Szalay, Astrophys. J. **304,** 15 (1986).

[132] V. De Luca, G. Franciolini, P. Pani, and A. Riotto, J. Cosmol. Astropart. Phys. 04 (2020) 052.

[133] I. Cholis, E. D. Kovetz, Y. Ali-Haïmoud, S. Bird, M. Kamionkowski, J. B. Muñoz, and A. Raccanelli, Phys. Rev. D **94,** 084013 (2016).

[134] Y.-F. Wang and A. H. Nitz, Astrophys. J. **912,** 53 (2021).

[135] K. Jedamzik, J. Cosmol. Astropart. Phys. 09 (2020) 022.

[136] M. Trashorras, J. García-Bellido, and S. Nesseris, Universe **7,** 18 (2021).

[137] M. Gorton and A. M. Green, J. Cosmol. Astropart. Phys. 08 (2022) 035.

[138] M. Petač, J. Lavalle, and K. Jedamzik, Phys. Rev. D **105,** 083520 (2022).

[139] V. De Luca, G. Franciolini, A. Riotto, and H. Veermäe, Phys. Rev. Lett. **129,** 191302 (2022).

[140] F. Ziparo, S. Gallerani, A. Ferrara, and F. Vito, Mon. Not. R. Astron. Soc. **517,** 1086 (2022).

[141] B. J. Kavanagh, D. Gaggero, and G. Bertone, Phys. Rev. D **98,** 023536 (2018).

[142] L. Liu, Z.-K. Guo, and R.-G. Cai, Phys. Rev. D **99,** 063523 (2019).

[143] M. Maggiore, *Gravitational Waves. Vol. 1: Theory and Experiments* (Oxford University Press, New York, 2007).

[144] I. Mandel and A. Farmer, Phys. Rep. **955,** 1 (2022).

[145] M. J. Benacquista and J. M. B. Downing, Living Rev. Relativity **16,** 4 (2013).

[146] Y.-B. Bae, C. Kim, and H. M. Lee, Mon. Not. R. Astron. Soc. **440,** 2714 (2014).

[147] C. L. Rodriguez, P. Amaro-Seoane, S. Chatterjee, and F. A. Rasio, Phys. Rev. Lett. **120,** 151101 (2018).

[148] M. Zevin, J. Samsing, C. Rodriguez, C.-J. Haster, and E. Ramirez-Ruiz, Astrophys. J. **871,** 91 (2019).

[149] M. Mapelli, Y. Bouffanais, F. Santoliquido, M. A. Sedda, and M. C. Artale, Mon. Not. R. Astron. Soc. **511,** 5797 (2022).

[150] J. Samsing, M. MacLeod, and E. Ramirez-Ruiz, Astrophys. J. **784,** 71 (2014).

[151] A. Nishizawa, E. Berti, A. Klein, and A. Sesana, Phys. Rev. D **94,** 064020 (2016).

[152] K. Breivik, C. L. Rodriguez, S. L. Larson, V. Kalogera, and F. A. Rasio, Astrophys. J. Lett. **830,** L18 (2016).

[153] A. Nishizawa, A. Sesana, E. Berti, and A. Klein, Mon. Not. R. Astron. Soc. **465,** 4375 (2017).

[154] M. Zevin, I. M. Romero-Shaw, K. Kremer, E. Thrane, and P. D. Lasky, Astrophys. J. Lett. **921,** L43 (2021).

[155] M. Favata, C. Kim, K. G. Arun, J. Kim, and H. W. Lee, Phys. Rev. D **105,** 023003 (2022).

[156] M. Kilic, C. Allende Prieto, W. R. Brown, and D. Koester, Astrophys. J. **660,** 1451 (2007).

[157] K. Strobel, C. Schaab, and M. K. Weigel, Astron. Astrophys. **350,** 497 (1999), https://adsabs.harvard.edu/full/1999A%26A...350..497S.

[158] J. M. Lattimer, Annu. Rev. Nucl. Part. Sci. **62,** 485 (2012).

[159] H. O. Silva, H. Sotani, and E. Berti, Mon. Not. R. Astron. Soc. **459,** 4378 (2016).

[160] Y. Suwa, T. Yoshida, M. Shibata, H. Umeda, and K. Takahashi, Mon. Not. R. Astron. Soc. **481,** 3305 (2018).

[161] S. L. Liebling and C. Palenzuela, Living Rev. Relativity **15,** 6 (2012).

[162] R. Ruffini and S. Bonazzola, Phys. Rev. **187,** 1767 (1969).

[163] M. Colpi, S. L. Shapiro, and I. Wasserman, Phys. Rev. Lett. **57,** 2485 (1986).

[164] V. Cardoso, E. Franzin, A. Maselli, P. Pani, and G. Raposo, Phys. Rev. D **95,** 084014 (2017); **95,** 089901(A) (2017).

[165] T. Binnington and E. Poisson, Phys. Rev. D **80,** 084018 (2009).

[166] T. Damour and A. Nagar, Phys. Rev. D **80,** 084035 (2009).

[167] T. Damour and O. M. Lecian, Phys. Rev. D **80,** 044017 (2009).

[168] P. Pani, L. Gualtieri, A. Maselli, and V. Ferrari, Phys. Rev. D **92,** 024010 (2015).

[169] P. Pani, L. Gualtieri, and V. Ferrari, Phys. Rev. D **92,** 124003 (2015).

[170] N. Gürlebeck, Phys. Rev. Lett. **114,** 151102 (2015).

[171] R. A. Porto, Fortschr. Phys. **64,** 723 (2016).

[172] A. Le Tiec and M. Casals, Phys. Rev. Lett. **126,** 131102 (2021).
[173] H. S. Chia, Phys. Rev. D **104,** 024013 (2021).
[174] A. Le Tiec, M. Casals, and E. Franzin, Phys. Rev. D **103,** 084021 (2021).
[175] L. Hui, A. Joyce, R. Penco, L. Santoni, and A. R. Solomon, J. Cosmol. Astropart. Phys. 04 (2021) 052.
[176] P. Charalambous, S. Dubovsky, and M. M. Ivanov, Phys. Rev. Lett. **127,** 101101 (2021).
[177] P. Charalambous, S. Dubovsky, and M. M. Ivanov, J. High Energy Phys. 05 (2021) 038.
[178] D. Pereñiguez and V. Cardoso, Phys. Rev. D **105,** 044026 (2022).
[179] E. E. Flanagan and T. Hinderer, Phys. Rev. D **77,** 021502 (2008).
[180] J. Vines, E. E. Flanagan, and T. Hinderer, Phys. Rev. D **83,** 084051 (2011).
[181] E. Poisson and C. Will, *Gravity: Newtonian, Post-Newtonian, Relativistic* (Cambridge University Press, Cambridge, England, 1953).
[182] K. Alvi, Phys. Rev. D **64,** 104020 (2001).
[183] A. Maselli, P. Pani, V. Cardoso, T. Abdelsalhin, L. Gualtieri, and V. Ferrari, Phys. Rev. Lett. **120,** 081101 (2018).
[184] https://apps.et-gw.eu/tds/?content=3&r=14065.
[185] https://apps.et-gw.eu/tds/ql/?c=16492.
[186] J. G. Rollins, E. Hall, C. Wipf, and L. McCuller, PyGWINC: Gravitational wave interferometer noise calculator, Astrophysics Source Code Library, record ascl:2007.020 (2020).
[187] V. Srivastava, D. Davis, K. Kuns, P. Landry, S. Ballmer, M. Evans, E. D. Hall, J. Read, and B. S. Sathyaprakash, Astrophys. J. **931,** 22 (2022).
[188] S. Borhanian, Classical Quantum Gravity **38,** 175014 (2021).
[189] https://dcc.cosmicexplorer.org/CE-T2000017/public.
[190] B. P. Abbott *et al.* (KAGRA, LIGO Scientific, and Virgo Collaborations), Living Rev. Relativity **23,** 3 (2020).
[191] https://dcc.ligo.org/LIGO-T2000012/public.
[192] L. S. Finn, Phys. Rev. D **46,** 5236 (1992).
[193] L. S. Finn and D. F. Chernoff, Phys. Rev. D **47,** 2198 (1993).
[194] C. Cutler and E. E. Flanagan, Phys. Rev. D **49,** 2658 (1994).
[195] E. Poisson and C. M. Will, Phys. Rev. D **52,** 848 (1995).
[196] E. Berti, A. Buonanno, and C. M. Will, Phys. Rev. D **71,** 084025 (2005).
[197] P. Ajith and S. Bose, Phys. Rev. D **79,** 084032 (2009).
[198] M. Vallisneri, Phys. Rev. D **77,** 042001 (2008).
[199] C. L. Rodriguez, B. Farr, W. M. Farr, and I. Mandel, Phys. Rev. D **88,** 084013 (2013).
[200] F. Iacovelli, M. Mancarella, S. Foffa, and M. Maggiore, Astrophys. J. Suppl. Ser. **263,** 2 (2022).
[201] https://github.com/CosmoStatGW/gwfast.

[202] U. Dupletsa, J. Harms, B. Banerjee, M. Branchesi, B. Goncharov, A. Maselli, A. C. S. Oliveira, S. Ronchini, and J. Tissino, Astron. Comput. **42,** 100671 (2023).
[203] M. L. Chan, C. Messenger, I. S. Heng, and M. Hendry, Phys. Rev. D **97,** 123014 (2018).
[204] Y. Li, I. S. Heng, M. L. Chan, C. Messenger, and X. Fan, Phys. Rev. D **105,** 043010 (2022).
[205] M. Pieroni, A. Ricciardone, and E. Barausse, Sci. Rep. **12,** 17940 (2022).
[206] L. Wade, J. D. E. Creighton, E. Ochsner, B. D. Lackey, B. F. Farr, T. B. Littenberg, and V. Raymond, Phys. Rev. D **89,** 103012 (2014).
[207] L. London, S. Khan, E. Fauchon-Jones, C. García, M. Hannam, S. Husa, X. Jiménez-Forteza, C. Kalaghatgi, F. Ohme, and F. Pannarale, Phys. Rev. Lett. **120,** 161102 (2018).
[208] C. Kalaghatgi, M. Hannam, and V. Raymond, Phys. Rev. D **101,** 103004 (2020).
[209] A. Buonanno, B. Iyer, E. Ochsner, Y. Pan, and B. S. Sathyaprakash, Phys. Rev. D **80,** 084043 (2009).
[210] P. Ajith, Phys. Rev. D **84,** 084037 (2011).
[211] C. K. Mishra, A. Kela, K. G. Arun, and G. Faye, Phys. Rev. D **93,** 084054 (2016).
[212] B. Moore, M. Favata, K. G. Arun, and C. K. Mishra, Phys. Rev. D **93,** 124061 (2016).
[213] K. Yagi and N. Yunes, Phys. Rep. **681,** 1 (2017).
[214] S. Husa, S. Khan, M. Hannam, M. Pürrer, F. Ohme, X. Jiménez Forteza, and A. Bohé, Phys. Rev. D **93,** 044006 (2016).
[215] S. Khan, S. Husa, M. Hannam, F. Ohme, M. Pürrer, X. Jiménez Forteza, and A. Bohé, Phys. Rev. D **93,** 044007 (2016).
[216] T. Dietrich, A. Samajdar, S. Khan, N. K. Johnson-McDaniel, R. Dudi, and W. Tichy, Phys. Rev. D **100,** 044003 (2019).
[217] G. Pratten, S. Husa, C. Garcia-Quiros, M. Colleoni, A. Ramos-Buades, H. Estelles, and R. Jaume, Phys. Rev. D **102,** 064001 (2020).
[218] G. Pratten *et al.*, Phys. Rev. D **103,** 104056 (2021).
[219] M. Mancarella, F. Iacovelli, and D. Gerosa, Phys. Rev. D **107,** L101302 (2023).
[220] A. H. Nitz and Y.-F. Wang, Phys. Rev. D **106,** 023024 (2022).
[221] R. Abbott *et al.* (LIGO Scientific, Virgo, and KAGRA Collaborations), arXiv:2212.01477.
[222] S. Young and A. S. Hamers, J. Cosmol. Astropart. Phys. 10 (2020) 036.
[223] K. Jedamzik, Phys. Rev. Lett. **126,** 051302 (2021).
[224] M. Tkachev, S. Pilipenko, and G. Yepes, Mon. Not. R. Astron. Soc. **499,** 4854 (2020).
[225] https://agenda.infn.it/event/23799/contributions/125718/ attachments/78986/102370/rome110221.pdf (2021).
[226] V. De Luca, G. Franciolini, P. Pani, and A. Riotto, Phys. Rev. D **102,** 043505 (2020).